===== **FIELDS, PARTICLES, AND NUCLEI** =====

Spontaneous Emission Probability for *M*1 Transition in a Dielectric Medium: ^{229m}Th(3/2$^+$, 3.5 ± 1.0 eV) Decay

E. V. Tkalya

Skobeltsyn Research Institute of Nuclear Physics, Moscow State University, Vorob'evy gory, Moscow, 119899 Russia
e-mail: tkalya@ibrae.ac.ru
Received March 15, 2000

The probability of spontaneous magnetic dipole emission in a transparent dielectric medium with refractive index *n* is shown to be n^3 times higher than in vacuum. The decay of a low-lying nuclear ^{229m}Th(3/2$^+$, 3.5 ± 1.0 eV) level in the ^{229}ThO$_2$ dielectric is discussed. © *2000 MAIK "Nauka/Interperiodica".*

PACS numbers: 23.20.Lv; 27.90.+b; 32.30.Jc; 32.70.Fw; 42.50.-p

An infinite dielectric medium influences the probability of spontaneous emission in the optical region (see, e.g., [1–3] and references therein). The probability W_m^{E1} of electric dipole transition in a medium with dielectric constant ϵ at an emission frequency ω (system of units $c = \hbar = 1$) can be expressed through the probability W_{vac}^{E1} of spontaneous decay in a vacuum by the relationship [1–3]

$$W_m^{E1} = \epsilon^{1/2} f^2(\epsilon) W_{vac}^{E1}. \tag{1}$$

Here, the function $f(\epsilon)$ relates the electric component $\mathbf{E}_m$ of a macroscopic electromagnetic field in a medium to the local electric field $\mathbf{E}_{loc}$ at the point where dipole is located. This function depends on the microscopic structure of the medium surrounding the emitting object, e.g., an atom. If the atom is placed in a sphere of small radius $R \ll \lambda = 2\pi/\omega$ inside which $\epsilon_{loc} = 1$, then $f(\epsilon) = 3\epsilon/(2\epsilon + 1)$ (the corresponding problem is solved in [4], chap. II; see also [1]). Other expressions for $f(\epsilon)$ can be found elsewhere [2, 5].

The factor $\epsilon^{1/2}$ in Eq. (1) arises as follows. Let us consider the following expression for the probability of electric dipole transition:

$$W_m^{E1} = 2\pi \left| \left\langle \left| \hat{\mathbf{d}} \cdot \hat{\mathbf{E}}_{loc}^+ \right| \right\rangle \right|^2 \rho_m(\omega), \tag{2}$$

where $\hat{\mathbf{d}}$ is the dipole moment operator of the emitting system and $\hat{\mathbf{E}}_{loc}^+$ is the electric-field creation operator related to the operator for the field in a medium via the expression $\hat{\mathbf{E}}_{loc}^+ = f(\epsilon)\hat{\mathbf{E}}_m^+$. The field operator $\hat{\mathbf{E}}_m^+$ and the density $\rho_m(\omega)$ of photon final states are renormal-

ized from the vacuum values according to the formulas [3]

$$\hat{\mathbf{E}}_m^+ = \frac{1}{\epsilon^{1/2}} \hat{\mathbf{E}}_{vac}^+, \quad \rho_m(\omega) = \epsilon^{3/2} \rho_{vac}(\omega). \tag{3}$$

The first of these relations immediately follows from the quantization rules for the electromagnetic field in a medium. For the gauge div$\mathbf{A} = 0$, the equation

$$\Delta \mathbf{A} - \epsilon \partial_t^2 \mathbf{A} = 0 \tag{4}$$

for the vector potential $\mathbf{A}$ follows from the Maxwell equations in a uniform dielectric medium with permeability equal to 1 in the absence of extrinsic currents and charges: curl$\mathbf{E} = -\partial_t\mathbf{H}$, div$\mathbf{H} = 0$, curl$\mathbf{H} = \partial_t\mathbf{D}$, and div$\mathbf{D} = 0$, where the electric and magnetic fields are defined via $\mathbf{A}$ in the standard way:

$$\mathbf{E} = -\partial_t\mathbf{A}, \quad \mathbf{H} = \text{curl}\mathbf{A}. \tag{5}$$

In the Maxwell equations, the electric induction is $\mathbf{D} = \epsilon\mathbf{E}$. We assume throughout this paper that the emission wavelength is much greater than the interatomic distances in the substance and that the ϵ value is independent of the coordinates.

The quantization of the electromagnetic field in a medium is carried out similarly to the quantization in vacuum. The vector potential can be written as an expansion in plane waves

$$\hat{\mathbf{A}}(\mathbf{r}, t) = \sum_{\mathbf{k}} \sum_{\lambda = 1, 2} (\hat{a}_{\mathbf{k}, \lambda} \mathbf{A}_{\mathbf{k}, \lambda} e^{-i\omega t} + \hat{a}_{\mathbf{k}, \lambda}^+ \mathbf{A}_{\mathbf{k}, \lambda}^* e^{i\omega t}), \tag{6}$$

where

$$\mathbf{A}_{\mathbf{k}, \lambda} = \mathbf{e}_{\mathbf{k}, \lambda} \sqrt{\frac{2\pi}{\epsilon\omega}} e^{i\mathbf{k}\mathbf{r}}, \tag{7}$$

$|\mathbf{k}| = \epsilon^{1/2}\omega$ [this immediately follows from Eq. (4)], $\mathbf{e}_{\mathbf{k}, \lambda}$ is the unit vector of plane wave polarization, and

$\sum_{\lambda = 1, 2}$ denotes the summation over two photon polarizations. The normalization volume is taken to be unity. The operators of photon creation and annihilation in Eq. (6) obey the ordinary commutation relations $[\hat{a}_{\mathbf{k}, \lambda} \hat{a}_{\mathbf{k}', \lambda'}] = [\hat{a}^+_{\mathbf{k}, \lambda} \hat{a}^+_{\mathbf{k}', \lambda'}] = 0$ and $[\hat{a}_{\mathbf{k}, \lambda} \hat{a}^+_{\mathbf{k}', \lambda'}] = \delta_{\mathbf{k}\mathbf{k}'} \delta_{\lambda\lambda'}$, and the field energy and momentum operators are expressed in terms of the creation and annihilation operators in the standard form $\hat{\mathcal{H}} = \sum_{\mathbf{k}} \sum_{\lambda = 1, 2} \omega(\hat{a}^+_{\mathbf{k}, \lambda} \hat{a}_{\mathbf{k}, \lambda} + 1/2)$ and $\hat{\mathbf{P}} = \sum_{\mathbf{k}} \sum_{\lambda = 1, 2} \mathbf{k}\hat{a}^+_{\mathbf{k}, \lambda} \hat{a}_{\mathbf{k}, \lambda}$.

As follows from Eqs. (6) and (7) and definition (5) of the electric field through the vector potential, the explicit form of the creation operator for an electric field with momentum $\mathbf{k}$ and energy ω in a medium is

$$\hat{\mathbf{E}}^+_{m_{\mathbf{k}, \lambda}} = -i\mathbf{e}^*_{\mathbf{k}, \lambda}\sqrt{\frac{2\pi\omega}{\epsilon}}e^{-i\mathbf{k}\mathbf{r}}\hat{a}^+_{\mathbf{k}, \lambda}. \tag{8}$$

This expression confirms the first of Eqs. (3).

The renormalization of phase volume is evident because, as mentioned above, $\mathbf{k}^2 = \epsilon\omega^2$ in matter. The $k^2 dk/d\omega$ value increases in a medium by a factor of $\epsilon^{3/2}$. In Eq. (2) for the probability, this factor not only compensates for a decrease in the electric field but also brings about $\epsilon^{1/2}$-type dependence of the emission probability on the dielectric constant, as indicated in Eq. (1).

The probability of magnetic dipole emission is calculated by the formula

$$W^{M1}_m = 2\pi\left|\left\langle\left|\hat{\boldsymbol{\mu}} \cdot \hat{\mathbf{H}}^+_{loc}\right|\right\rangle\right|^2 \rho_m(\omega), \tag{9}$$

where $\hat{\boldsymbol{\mu}}$ is the magnetic dipole moment operator of the emitting system. The operator $\hat{\mathbf{H}}^+_{loc}$ of a local magnetic field obviously coincides with the field operator $\hat{\mathbf{H}}^+_m$, because we consider a nonmagnetic medium (see [4], chap. IV and [1]). Using Eqs. (5)–(7), one can easily obtain

$$\hat{\mathbf{H}}^+_{m_{\mathbf{k}, \lambda}} = -i[\mathbf{k} \times \mathbf{A}^*_{\mathbf{k}, \lambda}]\hat{a}^+_{\mathbf{k}, \lambda}$$
$$= -i[\mathbf{n_k} \times \mathbf{e}^*_{\mathbf{k}, \lambda}]\sqrt{2\pi\omega}e^{-i\mathbf{k}\mathbf{r}}\hat{a}^+_{\mathbf{k}, \lambda}, \tag{10}$$

where $\mathbf{n_k}$ is the unit vector directed along the momentum $\mathbf{k}$.

Substituting $\hat{\mathbf{H}}^+_{m_{\mathbf{k}, \lambda}}$ from Eq. (10) and $\rho_m(\omega)$ from Eq. (3) into Eq. (9), we immediately obtain for the magnetic dipole emission

$$W^{M1}_m = \epsilon^{3/2}W^{M1}_{vac}. \tag{11}$$

Since the refractive index $n = \epsilon^{1/2}$ [4], the probability of $M1$ emission increases in a medium by a factor of n^3.

A comparison of Eqs. (8) and (10) for the operators $\hat{\mathbf{E}}^+_m$ and $\hat{\mathbf{H}}^+_m$, respectively, indicates that the well-known relationship $\epsilon^{1/2}\mathbf{E}_m = [\mathbf{H}_m \times \mathbf{n_k}]$ for the electric and magnetic components is fulfilled (see [4], chap. IX). Thus, it is not surprising that Eq. (11) relating the probability of magnetic dipole emission in a medium to the probability of transition in vacuum differs noticeably from analogous Eq. (1) for electric dipole emission. This point has received special attention in this study. The result expressed by Eq. (11) is inconsistent with the conclusions drawn in [1], where Eq. (6.24), an analogue of Eq. (11) in this work, includes the factor $\epsilon^{1/2}$ instead of $\epsilon^{3/2}$. This misunderstanding is associated with the fact that one should substitute $|\mathbf{k}| = \epsilon^{1/2}\omega$ for the momentum in the formula $[\nabla \times f_k(0)]_{diel} = \mathbf{k} \times \hat{\mathbf{e}}_{k, \mu}/\sqrt{\epsilon V}$ presented on p. 486 in [1] for the magnetic field amplitude. Indeed, the first terms in the expansion of the field $f_k(\mathbf{r})$ (an analogue of the vector potential $\mathbf{A}_{\mathbf{k}, \lambda}$), viz., the functions $\hat{\mathbf{e}}_{k, \mu} \exp(i\mathbf{k}\mathbf{r})/(\epsilon V)^{1/2}$ in Eqs. (6.17) and (6.20) in [1] are, as the authors of [1] state themselves, the solutions of Eq. (6.15) without the nonhomogeneous part. In other words, the indicated functions are the solutions of the homogeneous equation $\epsilon(\omega^2/c^2)\mathbf{f}_k(\mathbf{r}) - \nabla \times [\nabla \times \mathbf{f}_k(\mathbf{r})] = 0$. For this equation, $\mathbf{k}^2 = \epsilon\omega^2$. As a result, the magnetic-field magnitude is not renormalized. Accordingly, the factor $\epsilon^{1/2}$ in Eq. (6.24) for the emission probability is replaced by $\epsilon^{3/2}$. It should be noted that this inaccuracy in a particular example of $M1$ transition does not belittle the merits of [1] as a whole.

Result (11) can also be obtained by a different method based on the properties of the retarded Green function.[1] It is known (see, e.g., [2]) that the probabilities of spontaneous $E1$ and $M1$ emissions can be expressed through the spectral functions of electric- and magnetic-field fluctuations $\langle\mathbf{E}(\mathbf{r}_1)\mathbf{E}(\mathbf{r}_2)\rangle_\omega$ and $\langle\mathbf{H}(\mathbf{r}_1)\mathbf{H}(\mathbf{r}_2)\rangle_\omega$, respectively, taken at $\mathbf{r}_1 = \mathbf{r}_2$. At a temperature well below ω, these functions have the form ([6], chap. VIII)

$$\langle\mathbf{E}^2\rangle_\omega = \frac{1}{n^2}\langle\mathbf{H}^2\rangle_\omega = 2\omega^3 n. \tag{12}$$

Since [2]

$$W^{E1}_m \propto \left\langle\left|\hat{\mathbf{d}}\right|\right\rangle^2\langle\mathbf{E}^2\rangle_\omega, \quad W^{M1}_m \propto \left\langle\left|\hat{\boldsymbol{\mu}}\right|\right\rangle^2\langle\mathbf{H}^2\rangle_\omega,$$

Eqs. (12) evidently confirm the above conclusion about the n^3 dependence of the probability of spontaneous magnetic dipole emission on the refractive index.

This conclusion may be of crucial importance for estimating the lifetime of the anomalously low-lying $3/2^+(3.5 \pm 1.0 \text{ eV})$ level of the ^{229}Th nucleus [7]. This level decays into the ground $5/2^+$ state via the $M1$ tran-

---

[1] In this approach, the local-field effects are not considered; i.e., we set $f(\epsilon) = 1$.

sition. In the isolated Th atom, the process of the third order in the electromagnetic coupling constant (the electronic bridge) should be the most probable decay channel [8]. However, thorium is a chemically active element. Its dioxide is the most abundant and stable chemical compound. ThO_2 is a dielectric with an energy gap of ca. 6 eV and refractive index $n \simeq 2$ for photons with energy 3.1 eV [9].

The energy gap of the ideal dielectric contains no electronic states. For this reason, the continuous states of the conduction band of $^{229}ThO_2$ should serve as intermediate states in the decay of the low-lying nuclear isomer through the electronic bridge. The mismatch of the corresponding nuclear and electronic transition energies exceeds 1 eV. Moreover, only the elastic electronic bridge, i.e., the $M1$ emission in the "second" electronic transition should be taken into consideration. The probability of such an electronic bridge is negligibly small [8].

As the result, a direct nuclear emission in the optical range may be the main decay channel for the low-lying $3/2^+$ $(3.5 \pm 1.0$ eV$)$ level in $^{229}ThO_2$. The decay probability for the isolated nucleus in a vacuum is given by the formula [10]

$$W_\gamma = \frac{8\pi}{[(2L+1)!!]^2} \frac{L+1}{L} \omega^{2L+1} B(E(M)L),$$

where L is the multipolarity and $B(E(M)L)$ is the reduced probability of the nuclear transition. The $B(M1; 3/2^+ \longrightarrow 5/2^+)$ value for the isomeric ^{229}Th transition of interest was obtained in [11]. Taking into account the Coriolis interaction between the rotational bands related to the isomeric and ground states, it was found in [11] that $B(M1; 3/2^+ \longrightarrow 5/2^+) \simeq 0.086\mu_N^2 \simeq 4.8 \times 10^{-2}$ Wu, where Wu stands for the Weisskopf units, $\mu_N = e/2m_p$ is the nuclear magneton, and m_p is the proton mass. Without regard for the medium effect, one has $T_{1/2} = \ln 2/W_\gamma \simeq 80$ min–8 h in the energy range $\omega = $ 4.5–2.5 eV. If the effect of a dielectric medium is taken into account, the decay probability in thorium dioxide should be modified according to Eq. (11). As a result, the most probable lifetime of the $3/2^+$ $(3.5 \pm 1.0$ eV$)$ state in $^{229}ThO_2$ will lie in the range 10 min–1 h. Note that this estimation is made under the assumption that $n \simeq 2$ not only for $\omega = 3.1$ eV, as in [9], but also over the entire energy range of 2.5–4.5 eV. The corresponding

numerical result can be refined with allowance made for the actual n value.

It is quite difficult to check the effect of an infinite dielectric medium on atomic emission. In this respect, the above analysis of the $3/2^+$ $(3.5 \pm 1.0$ eV$)$ level decay in $^{229}ThO_2$ may be useful for the experimental corroboration (or refutation) of the relationship between the decay in a vacuum and in a medium in the form of Eqs. (1) and (11).

REFERENCES

1. R. J. Glauber and M. Lewenstein, Phys. Rev. A **43**, 467 (1991).
2. S. M. Barnett, B. Huttner, and R. Loudon, Phys. Rev. Lett. **68**, 3698 (1992).
3. E. Yablonovitch, T. J. Gmitter, and R. Bhat, Phys. Rev. Lett. **61**, 2546 (1988).
4. L. D. Landau and E. M. Lifshitz, *Course of Theoretical Physics. Vol. 8. Electrodynamics of Continuous Media* (Nauka, Moscow, 1982; Pergamon, New York, 1984).
5. V. M. Agranovich and M. D. Galanin, *Electronic Excitation Energy Transfer in Condensed Matter* (Nauka, Moscow, 1978; North-Holland, Amsterdam, 1982).
6. L. D. Landau and E. M. Lifshitz, *Course of Theoretical Physics. Vol. 9*; E. M. Lifshitz and L. P. Pitaevskii, *Statistical Physics* (Nauka, Moscow, 1976; Pergamon, Oxford, 1980), Part 2.
7. R. G. Helmer and C. W. Reich, Phys. Rev. C **49**, 1845 (1994).
8. V. F. Strizhov and E. V. Tkalya, Zh. Éksp. Teor. Fiz. **99**, 697 (1991) [Sov. Phys. JETP **72**, 387 (1991)].
9. A. I. Sviridova and I. V. Suĭkovskaya, Opt. Spektrosk. **22**, 940 (1967).
10. I. Aĭzenberg and V. Graĭner, *Mechanisms of Nucleus Excitation. Electromagnetic and Weak Interactions* (Atomizdat, Moscow, 1973).
11. A. M. Dykhne and E. V. Tkalya, Pis'ma Zh. Éksp. Teor. Fiz. **67**, 233 (1998) [JETP Lett. **67**, 251 (1998)].

Translated by R. Tyapaev

===== **PLASMA, GASES** =====

Suppression of the Magnetic Surface Shift
by Plasma Rotation in a Tokamak

V. I. Il'gisonis and Yu. I. Pozdnyakov

Institute of Nuclear Fusion, Russian Research Centre Kurchatov Institute, pl. Kurchatova 1, Moscow, 123182 Russia
e-mail: vil@nfi.kiae.ru
Received March 16, 2000

The equilibrium of a toroidally rotating plasma in an axisymmetric tokamak-like system is considered. The equilibrium equation is represented in the form of the Grad–Shafranov equation in which, in contrast to the static case (with no plasma rotation), the plasma pressure depends on both the flux surface label and major radius. It is shown that the dependence of the pressure on the major radius makes it possible to choose the profile of the plasma rotation velocity so as to minimize the effect of the plasma pressure on the shift of the flux surfaces, in which case it might be anticipated that the maximum pressure of the confined plasma will be higher. This result was derived analytically and tested numerically for a number of typical tokamak configurations with a fixed plasma boundary. © *2000 MAIK "Nauka/Interperiodica"*.

PACS numbers: 52.30.Bt; 52.55.Fa

At present, the most advanced devices for magnetic confinement of high-temperature plasmas are tokamaks, which are axisymmetric ($\partial/\partial\xi \longrightarrow 0$ in cylindrical coordinates $\{r, z, \xi\}$) systems with toroidally nested magnetic flux surfaces $\Psi(r, z) = \text{const}$ such that $\mathbf{B} \cdot \nabla\Psi = 0$. Although the theory of static (with the mean plasma mass velocity $\mathbf{v} = 0$) plasma equilibrium in tokamaks is well developed (see, e.g., the well-known reviews [1, 2]), in order to adequately model tokamak experiments, it should be supplemented by attention to plasma rotation, which is routinely observed in large tokamaks, especially in operating modes with high-power neutral beam injection. The plasma rotation velocity can be on the order of sonic speed; near the magnetic axis, the plasma rotates preferentially in the toroidal direction.

That plasma rotation is an important issue in describing toroidal plasma states was recognized a long time ago (see, e.g., [3–5] and the literature cited therein). During the 1980s and 1990s, the problem of the equilibrium of a rotating plasma was treated in a fairly large number of papers (see, e.g., [6–9] and the literature cited therein). The interest in this problem is attributable in part to the circumstance that plasma rotation plays a key role in achieving regimes with enhanced plasma confinement.

The equilibrium configuration of an arbitrarily rotating plasma is governed by five flux-surface functions, in contrast to the static case, in which only two functions are required: the plasma pressure $p = p(\Psi)$ and poloidal current $I = I(\Psi)$. In this paper, in order to minimize the plasma pressure–induced shift of the magnetic flux surfaces with respect to the magnetic axis (the so-called Shafranov shift $\triangle$) [10], we use freedom in the choice of the flux-surface functions, specifically, the velocity profile of the toroidal plasma rotation.

The Shafranov shift results from the well-known ballooning effect: an increase in the plasma pressure inside the plasma column causes the plasma to extend preferentially outward from the major axis of the torus. In tokamaks, the maximum achievable values of the parameter β (the ratio of the plasma pressure to the magnetic field pressure) are limited by the condition $\triangle \lesssim a_b$ (where a_b is the characteristic minor radius of the plasma column) imposed by the effect of the Shafranov shift. In actuality, the equilibrium beta limit is even lower: it is achieved when the Shafranov shift $\triangle$, which is associated with finite plasma pressure, becomes so significant that a separatrix appears in the plasma column and the nested structure of the magnetic surfaces is broken. Consequently, we may expect that suppressing the Shafranov shift will raise the maximum possible β-values, which is a very important issue for controlled fusion research.

We consider the time-independent MHD equations in the form

$$\rho(\mathbf{v} \cdot \nabla)\mathbf{v} + \nabla p + [\mathbf{B} \times \text{curl}\mathbf{B}] = 0, \qquad (1)$$

$$\text{curl}[\mathbf{v} \times \mathbf{B}] = 0, \qquad (2)$$

$$\text{div}\mathbf{B} = 0, \qquad (3)$$

$$\text{div}(\rho\mathbf{v}) = 0, \qquad (4)$$

$$\mathbf{v} \cdot \nabla S = 0. \qquad (5)$$

For

$$S = p/\rho^{\gamma}, \qquad (6)$$

Eq. (5) is an adiabatic equation with the adiabatic index γ. The axisymmetric magnetic field that generates a family of nested toroidal flux surfaces $\Psi(r, z) = \text{const}$ and satisfies Eq. (3) can generally be represented as

$$\mathbf{B} = \nabla\zeta \times \nabla\Psi + I(r, z)\nabla\zeta. \quad (7)$$

The quantity Ψ in (7) has the meaning of the poloidal magnetic flux. Equation (2) implies that the plasma streamlines should also lie on the flux surfaces, so that, according to (5), the entropy function S depends on the flux surface label $S = S(\Psi)$.

We restrict ourselves to considering purely toroidal plasma rotation,

$$\mathbf{v} = \omega(r, z)r^2\nabla\zeta, \quad (8)$$

in which case the scalar equilibrium equation has the form

$$\Delta^*\Psi + II'_\Psi + r^2\rho(H'_\Psi + r^2\omega\omega'_\Psi - T\eta'_\Psi) = 0, \quad (9)$$

where

$$H(\Psi) = h - \frac{\omega^2 r^2}{2}; \quad I = I(\Psi). \quad (10)$$

We can see that I, ω, and H are flux-surface functions, i.e., $I(r, z) = I(\Psi(r, z))$, etc. Applying the thermodynamic approach and using Eq. (6), we can express p and ρ as functions of the enthalpy h in (10):

$$\rho = \left(\frac{h}{\alpha S}\right)^{\alpha-1}; \quad p = \left(\frac{h}{\alpha S^{\frac{\alpha-1}{\alpha}}}\right)^\alpha \quad \left(\alpha = \frac{\gamma}{\gamma-1} > 1\right). \quad (11)$$

Thus, the MHD equilibrium of a toroidally rotating plasma is determined by the four independent flux-surface functions $I = I(\Psi)$, $\omega = \omega(\Psi)$, $H = H(\Psi)$, and $S = S(\Psi)$, where the flux function $\Psi(r, z)$ satisfies Eq. (9), which can be represented in the form of the conventional Grad–Shafranov equation:

$$\Delta^*\Psi + II'_\Psi + r^2\frac{\partial p}{\partial\Psi} = 0. \quad (12)$$

In accordance with (10) and (11), we have

$$p = p(\Psi, r) = \left(\frac{H + \frac{1}{2}\omega^2 r^2}{\alpha S^{(\alpha-1)/\alpha}}\right)^\alpha, \quad (13)$$

$$\rho = \rho(\Psi, r) = \left(\frac{H + \frac{1}{2}\omega^2 r^2}{\alpha S}\right)^{\alpha-1}. \quad (14)$$

We note that, if the thermal conductivity along the magnetic field is high, then, instead of the adiabatic equation (5), it may be worthwhile to use the condition

for the temperature to be constant along the magnetic field lines, $T = T(\Psi)$. In this case, we have [7]

$$\rho(\Psi, r) = \rho_0(\Psi)\exp\left(\frac{\omega^2 r^2}{2T}\right),$$
$$p(\Psi, r) = \rho_0(\Psi)T(\Psi)\exp\left(\frac{\omega^2 r^2}{2T}\right), \quad (15)$$

so that the equilibrium equation again reduces to Eq. (12).

The sole difference between Eq. (12) and the conventional Grad–Shafranov equation is that it contains the partial (rather than ordinary) derivative with respect to Ψ, because the pressure of a rotating plasma depends explicitly not only on the flux surface label but also, according to (13) and (15), on the radial coordinate r. We will use this circumstance in further analysis.

We turn to Eq. (12) to consider the structure of the flux surfaces near the magnetic axis ($r = R$, $z = 0$), assuming that the aspect ratio is large, $R/a \gg 1$. Following Zakharov and Shafranov [2], we work in the approximation of nearly circular flux surfaces determined by

$$\Psi = \Psi(a): r \approx R + \triangle(a) - (a - \varepsilon(a)\cos2\theta - \ldots)\cos\theta,$$
$$z \approx (a - \varepsilon(a)\cos2\theta - \ldots)\sin\theta \quad (16)$$

and specify the hierarchy $\triangle(a) \sim a^2/R$, $\varepsilon(a) \sim a(a/R)^2$, etc. In this approach, the left-hand side of the equilibrium equation (12) contains the full set of harmonics of the poloidal angle θ. The coefficients in front of each of the poloidal harmonics should be equated to zero independently. To leading order in a/R, the lowest harmonics satisfy the equations

$$\frac{dJ}{da} = \frac{a}{R}II'_\Psi + \frac{a}{R}\left(r^2\frac{\partial p}{\partial\psi}\right)\bigg|_{r=R}; \quad (17)$$

$$\frac{a}{J}\frac{d}{da}\left(\frac{J^2}{a}\frac{d\triangle(a)}{da}\right) = -\frac{J}{R} - 2a^2\left(\frac{\partial}{\partial r^2}\left(r^2\frac{\partial p}{\partial\Psi}\right)\right)\bigg|_{r=R}; \quad (18)$$

$$\frac{a}{J}\frac{d}{da}\left(J^2\frac{\varepsilon'}{a}\right) - 3\frac{J}{a^2}\varepsilon + \frac{3}{2}\frac{d}{da}(J\triangle'^2) - J\left(\frac{\triangle'}{R} + \frac{a}{R^2} + \frac{3}{2}\frac{\triangle'^2}{a}\right)$$
$$- a^2 R\left(\frac{\partial}{\partial r^2}\left(r\frac{\partial}{\partial r^2}\left(r^2\frac{\partial P}{\partial\Psi}\right)\right)\right)\bigg|_{r=R} = 0, \quad (19)$$

where the prime denotes the derivative with respect to a so that $(\ldots)'_\Psi = d/d\Psi \approx -a(\ldots)'/RJ$. Equation (17) determines the toroidal current $J(a) \approx -a\Psi'/R$, Eq. (18) determines the shift $\triangle(a)$, Eq. (19) determines the ellipticity $\varepsilon(a)$, and so on.

Integrating Eq. (18) for the Shafranov shift by analogy with [2], we obtain

$$\triangle'(a) = -\frac{a}{R}\left(\frac{1}{2}l_i(a) + \tilde{\beta}_J(a)\right), \qquad (20)$$

where

$$l_i(a) = \frac{2}{J^2(a)}\int_0^a \frac{J^2(x)}{x}dx,$$

$$\tilde{\beta}_J(a) = \frac{4}{J^2(a)}\int_0^a\left[\left(p(R, x) + R^2\frac{\partial p}{\partial r^2}(r, x)\bigg|_{r=R}\right)\right. \qquad (21)$$

$$\left. -\left(p(R, a) + R^2\frac{\partial p}{\partial r^2}(r, a)\bigg|_{r=R}\right)\right]xdx.$$

We can readily see that, according to (20), the Shafranov shift, as a function of pressure, is determined by the parameter $\tilde{\beta}_J$. When there is no rotation, we have $(\partial/\partial r^2)(r^2\partial p/\partial\Psi) \longrightarrow p'$ and

$$\tilde{\beta}_J \longrightarrow \beta_J = \frac{4}{J^2}\int_0^a(p(x) - p(a))xdx.$$

This quantity is definitely nonzero for any pressure profile with a maximum in the center and decreasing towards the plasma edge [formally, we have $\beta_J = 0$ for $p(a) = $ const, in which case, however, the plasma equilibrium is ensured by a current layer that forms at the plasma edge and makes a comparable integral contribution to the shift (20)]. For a rotating plasma, the parameter $\tilde{\beta}_J$ can be made small by holding the quantity

$$\frac{\partial}{\partial r^2}(r^2 p)\bigg|_{r \approx R}$$

fixed, in which case the plasma pressure $p(\Psi, r)$ defined by (13) should satisfy the condition

$$(\mathscr{F}_1(\Psi) + \mathscr{F}_2(\Psi)R^2)^\alpha + \alpha R^2\mathscr{F}_2(\Psi)$$
$$\times (\mathscr{F}_1(\Psi) + \mathscr{F}_2(\Psi)R^2)^{\alpha-1} \approx \text{const} \Rightarrow \tilde{\beta}_J(a) \approx 0, \qquad (22)$$

where

$$p(\Psi, r) = (\mathscr{F}_1(\Psi) + \mathscr{F}_2(\Psi)r^2)^\alpha,$$

$$\mathscr{F}_1(\Psi) = \frac{H}{\alpha S^{(\alpha-1)/\alpha}}, \quad \mathscr{F}_2(\Psi) = \frac{\omega^2}{2\alpha S^{(\alpha-1)/\alpha}}.$$

For definiteness, we assume a fixed plasma boundary $\Psi(r, z) = \Psi_b$. This approximation is quite suitable for modeling real experiments and can be applied not only when the sizes of the plasma confinement region are governed by the conducting wall or by the limiter. In a divertor-equipped tokamak, the position of the boundary flux surface (the separatrix) is effectively controlled by varying the external poloidal field. If the plasma pressure vanishes at the boundary, $p(\Psi_b, r) \approx 0$, then condition (22) clearly cannot be satisfied for any Ψ. However, this is not required, because the position of the boundary surface is prescribed *a priori* and the velocity at which the edge plasma rotates is of no importance. It is desirable to satisfy condition (22) in the region where the Shafranov shift is maximum, namely, in the central plasma region. Expanding condition (22) in powers of a, we can use the pressure profile or the $H(\Psi)$ profile in order to find such a profile of the angular velocity of toroidal plasma rotation that would minimize the Shafranov shift. Using the zero subscript to denote the values of the quantities at $a = 0$, we obtain the relationship

$$\mathscr{F}'_{20}R^2 \approx -\mathscr{F}'_{10}\frac{\mathscr{F}_{10} + \alpha R^2\mathscr{F}_{20}}{2\mathscr{F}_{10} + (\alpha + 1)R^2\mathscr{F}_{20}}. \qquad (23)$$

We can see that the absolute value of the plasma rotation velocity at the center of the plasma column is unimportant. Condition (23) can even be satisfied when the plasma at the magnetic axis does not rotate, i.e., when $\mathscr{F}_{20} = 0$, in which case the radial derivative of the plasma rotation velocity is determined by the universal relationship

$$\mathscr{F}'_{20}R^2 \approx -\mathscr{F}'_{10}/2; \qquad (24)$$

i.e., there is no dependence on either $\mathscr{F}_{10}$ or α.

Condition (22) can also be interpreted in a different manner. Let us address the question of how high the toroidal rotation velocity of the plasma at a radius $r = r_1$(at which the plasma pressure is $p \approx p_1$) should be in order to minimize the Shafranov shift, provided that the plasma does not rotate at the magnetic axis. To answer this question requires insignificant algebra:

$$v_1 = (\omega r)_1 \approx c_S\left(\frac{2}{\gamma}\frac{p_0 - p_1}{p_1}\right)^{1/2}, \qquad (25)$$

where c_S is the speed of sound at the radius denoted by the subscript 1.

We checked the above conclusions numerically by running a fixed-boundary code capable of calculating equilibrium magnetic and plasma configurations in tokamaks from Eqs. (12) and (13). To save space, we omit the details of the computations and note only that an essentially complete suppression of the Shafranov shift (or a significant reduction—by a factor of 6 to 8—in configurations with a highly elliptical plasma boundary) was reliably captured by the code even at an aspect ratio of about 3, i.e., even when the asymptotic expansion in powers of a/R may lead to significant errors. We also found that the maximum possible β values were higher than those in the static case by a factor of 1.6 to 2.5. Hence, we can conclude that the effect under dis-

cussion is pronounced enough to be not only captured numerically but also observed experimentally.

On the other hand, we emphasize that this effect cannot *in principle* be described by the familiar analytic solutions to the equilibrium equation (9), e.g., by the Maschke–Perrin solution [7], which is often cited in the literature. In [7], the flux-surface functions $H(\Psi)$ and $\omega(\Psi)$ for which $\mathcal{F}_1/\mathcal{F}_2 = \text{const}$ and $\mathcal{F}_{1,2} \sim \Psi^{1/\alpha}$ were chosen in such a way that the derivative $\partial p/\partial \Psi$ depends only on r. Although this choice makes it possible to solve Eq. (12) analytically, it contradicts our condition

$$\frac{\partial}{\partial r^2}\left(r^2 \frac{\partial p}{\partial \Psi} \right) \approx 0$$

and its consequences (23) and (24). This circumstance explains why the plasma rotation in the Maschke–Perrin solution and in analogous solutions, as a rule, has an unfavorable effect on the parameters of the confined plasma.

In conclusion, we summarize the main results of our study.

In the case of purely toroidal plasma rotation, the MHD equilibrium equation can be written in the form of the Grad–Shafranov equation in which the total derivative $dp/d\Psi$ should be replaced with the partial derivative $\partial p/\partial \Psi$.

The shift of the flux surfaces is described by a formula similar to that for the Shafranov shift.

In contrast to the static case, the plasma pressure–induced shift of the flux surfaces can be substantially suppressed (and, in some cases, even eliminated completely) by an appropriate choice of the toroidal velocity profile, no matter how high the absolute value of the rotation velocity.

In order to minimize the Shafranov shift of the flux surfaces in the case of a pressure profile with a maximum in the center and decreasing towards the plasma edge, it is necessary to ensure that the toroidal plasma rotation velocity increases with distance from the magnetic axis.

The operating modes with a reduced shift of the flux surfaces make it possible to achieve higher equilibrium β values.

REFERENCES

1. L. S. Solov'ev and V. D. Shafranov, in *Reviews of Plasma Physics*, Ed. by M. A. Leontovich (Atomizdat, Moscow, 1967; Consultants Bureau, New York, 1970), Vol. 5.

2. L. E. Zakharov and V. D. Shafranov, in *Reviews of Plasma Physics*, Ed. by M. A. Leontovich and B. B. Kadomtsev (Énergoatomizdat, Moscow, 1982; Consultants Bureau, New York, 1987), Vol. 11.

3. H. Grad, Rev. Mod. Phys. **32**, 830 (1960).

4. H. P. Zehrfeld and B. J. Green, Nucl. Fusion **12**, 569 (1972).

5. A. I. Morozov and L. S. Solov'ev, in *Reviews of Plasma Physics*, Ed. by M. A. Leontovich (Atomizdat, Moscow, 1974; Consultants Bureau, New York, 1986), Vol. 8.

6. E. Hameiri, Phys. Rev. A **27**, 1259 (1983).

7. E. K. Maschke and H. Perrin, Plasma Phys. **22**, 579 (1980).

8. W. Kerner and S. Tokuda, Z. Naturforsch. A **42**, 1154 (1987).

9. H. Tasso and G. N. Throumoulopoulos, Phys. Plasmas **5**, 2378 (1998).

10. V. S. Mukhovatov and V. D. Shafranov, Nucl. Fusion **11**, 605 (1971).

Translated by O. Khadin

=== **CONDENSED MATTER** ===

On the Mechanism of the Photodomain Effect in Ferroelectrics[1]

T. M. Batirov*, D. Dimos**, E. Doubovik*, R. Djalalov*, and V. M. Fridkin*

* Shubnikov Institute of Crystallography, Russian Academy of Sciences, Leninskiĭ pr. 59, Moscow, 117333 Russia
** Sandia National Laboratories, Albuquerque, N.M. 87185-580, USA
e-mail: fridkin@ns.crys.ras.ru
Received March 1, 2000

The influence of nonequilibrium electrons on the domain structure and switching of ferroelectrics (photodomain effect) has been investigated in ferroelectric crystals and ceramics. In the present paper, this effect is observed and explained as a result of the domain walls screening in frame of Yshibashi–Takagi theory. © 2000 MAIK "Nauka/Interperiodica".

PACS numbers: 77.80.Dj

The influence of intrinsic light on the equilibrium domain structure, on the kinetics of its switching, and on the properties directly related to the domain structure (e.g., the pyroelectric charge, electromechanical hysteresis, etc.) was called the photodomain effect [1]. The photodomain (PD) effect was first observed in SbSI crystals [2]. The first observations of the PD were performed by indirect methods, such as the influence of illumination on the pyroelectric current and Barkhausen discontinuity [3, 4]. Later, the PD effect was observed by direct observations of the intrinsic illumination on domain structure in SbSI and $BaTiO_3$ crystals [5, 6]. In [7–10], the PD effect was observed in PZT and PZLT ferroelectric films and explained by the mechanism of the screening of 90° domain walls (or the walls with a boundary which is not parallel to the external fields) by nonequilibrium carriers. It was shown that illumination of PZT or PZLT films in the intrinsic optical region leads to suppression of the switchable polarization in the external field. In the present paper, we show that the Yshibashi–Takagi model (YT model) [11] permits one to explain the PD effect by the mechanism of domain-wall screening.

In the YT model, four parameters are required to describe the polarization reversal. The probability of nucleation per unit volume and unit time is given by R; the initial radius of a nucleus, by r_c; the domain-wall velocity, by ν; and the dimensionality of growth, by d.

The fraction of switched volume to total volume is given by $Q(t) = 1 - q(t)$, where $q(t)$ is suppression. The switching current is then found by

$$i(t) = 2P_s \frac{dQ(t)}{dt} = -2P_s \frac{dq(t)}{dt}, \qquad (1)$$

where P_s is the spontaneous polarization per unit volume. Thus,

$$P_s(t)/P_s(0) = 1 - q(t). \qquad (2)$$

The YT model gives the following expression for $q(t)$ [11]:

$$\ln q(t) = -\frac{C_d R}{\nu(d+1)}[(r_c + \nu \cdot t)^{d+1} - r_c^{d+1}], \qquad (3)$$

where $C_d = 2$, π, and $4\pi/3$ for $d = 1, 2$, and 3, respectively. The switching current is given by

$$i(t) = 2P_s C_d R (r_c + \nu t)^d$$
$$\times \exp\left[-\frac{C_d R}{\nu(d+1)}[(r_c + \nu t)^{d+1} - r_c^{d+1}]\right]. \qquad (4)$$

If the size of a nucleus is negligibly small on the scale of the system, as is usually the case, then Eqs. (3) and (4) have the form

$$\ln q(t) = -\frac{\theta}{d+1} t^{d+1}, \qquad (5)$$

$$i(t) = P_s \theta \cdot t^d \exp\left[-\frac{\theta}{d+1} t^{d+1}\right], \qquad (6)$$

where $\theta = C_d R \nu^d$.

This model was successfully applied to thin ferroelectric films [12, 13].

Upon illumination of the ferroelectric crystal (or film), the nonequilibrium electrons influence the kinetics of the ferroelectric switching. Within the framework of the YT model, the illumination, in principle, changes R, r_c, and ν. The change in r_c is evident, because the free surface energy of the domain depends on the concentration of photoelectrons (due to the screening). The illumination may also increase the nucleation rate R due to the trapping of photoelectrons. The velocity of the wall ν also depends on the concentration of photoelectrons.

---

[1] This article was submitted by the authors in English.

We shall suppose that at $t = \tau_m$, where $\tau_m = \varepsilon/4\pi\sigma$ is Maxwellian time, the switching is finished due to the screening of the walls (see Fig. 1). Thus, we can obtain from Eq. (3) the value $q(t = \tau_m)$, which characterizes the unswitched volume of the crystal or film, see Eq. (2). We shall consider the value of $q(t = \tau_m)$ as the degree of photoinduced hysteresis suppression (or PD effect).

Substituting $t = \tau_m$ in Eq. (3), we obtain

$$q(t) = \exp\left\{-\frac{C_d R}{\nu(d+1)}[(r_c + \nu\tau_m)^{d+1} - r_c^{d+1}]\right\}, \quad (7)$$

where $\tau_m = \varepsilon/4\pi\sigma_{ph} = \varepsilon/4\pi\sigma_{ph}^0 \cdot I$ (I is light intensity in the case of the linear dependence $\sigma_{ph} = \sigma_{ph}(I)$, $\sigma_{ph} \gg \sigma_d$; σ_{ph} is photoconductivity; and σ_d is dark conductivity).

We can see from Eqs. (3) and (7) that at $t = 0$ $q(0) = 1$ and $P_s(t) = P_s(0)$. At $t = \tau_m$, $q(\tau_m) < 1$ and, correspondingly, $P_s(\tau_m) < P_s(0)$. Thus, we obtain the PD effect. It is seen from Eq. (7), that the PD effect increases with the light intensity. Eq. (7) does not describe the kinetics of this effect, because we did not take into account the dependence of R, r_c, and ν on the light intensity. If we neglect this dependence, Eq. (7) will describe the dependence of photoinduced hysteresis suppression on the time of illumination. Of course, this approach is valid if the Maxwellian time is comparable with the switching time.

If the size of a nucleus is negligibly small in comparison with grown and screened domains ($r_c \ll \nu\tau_m$), the photoinduced hysteresis suppression is given by Eq. (8):

$$q(\tau_m) = \exp\left[-\frac{C_d R \nu^d}{d+1}\tau_m^{d+1}\right]. \quad (8)$$

It is seen from Eq. (8) that $q(\tau_m) \sim \exp[-\text{constant} \cdot \tau_m^{d+1}]$ and the effect increases with light intensity. From the dependence $q(\tau_m) = q(I)$, we can determine, in principle, the dimensionality of the domain growth d.

The effect of photoinduced hysteresis suppression is determined by $q(\tau_m)$. The dependence of q on the light intensity I is given by Eq. (8), if we substitute in Eq. (8) the value τ_m:

$$\tau_m = \varepsilon/4\pi\sigma_{ph}(I).$$

If the photoconductivity σ_{ph} linearly depends on the light intensity I, i.e.,

$$\sigma_{ph} = \sigma_{ph}^0 \cdot I,$$

the dependence $q = q(I)$ is given by Eq. (9),

$$q = \exp\left[-\frac{C_d R \nu^d}{d+1}\left(\frac{\varepsilon}{4\pi\sigma_{ph}^0}\right)^{d+1} I^{-(d+1)}\right]. \quad (9)$$
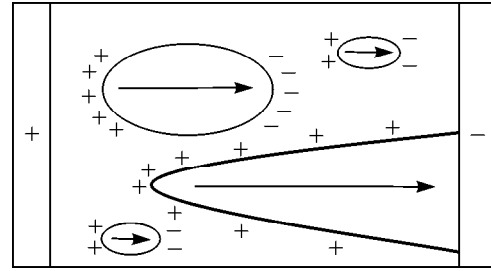
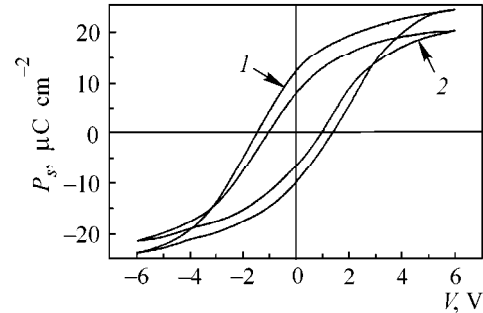**Fig. 1.** Screening of the domain walls by nonequilibrium carriers.

Fig. 2. The effect of photoinduced hysteresis suppression in PZT: (*1*) the initial hysteresis loop; (*2*) the suppressed hysteresis loop; $\lambda \cong 368$ mm, $I = 4.5$ mW cm^{-2}, $V = 3$ V.

It is seen from Eq. (9) that the effect of the photoinduced hysteresis suppression q increases with light intensity I.

The experimental data [9, 10] show that the illumination of PZT and PZLT ferroelectric ceramics in the intrinsic optical region leads to an increase in q. This effect of hysteresis suppression may be explained qualitatively by the model developed. For the numerical comparison, we need the experimental investigation of q as a function of the light intensity.

We investigated PZT thin films of thickness $l \cong 3\mu$, which were prepared using the sol–gel deposition technique [14, 15]. This technology provides a single-phase perovskite structure. As a semitransparent electrode, we used Pt (150 Å) sputter-deposited on the film. As a second electrode, we used Pt sputter-deposited on an oxidized silicon wafer. The illumination of the film was performed through the semitransparent electrode. The illumination of the films was performed with a Xe lamp and a ZMR monochromator in the spectral region of 300–800 nm. The low-frequency Sawyer–Tower system was used for the measurements of the dielectric hysteresis loops ($f = 70$ Hz).

The effect of photoinduced hysteresis suppression is shown in Fig. 2. The initial hysteresis loop is shown by curve *1*, the photoinduced hysteresis loop is shown by curve *2*, and the effect of the photoinduced hysteresis suppression q is determined by Eq. (2). In accordance
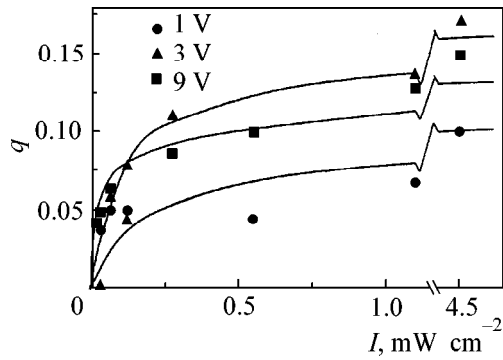
Fig. 3. Experimental dependence of q on the light intensity I for different voltages.
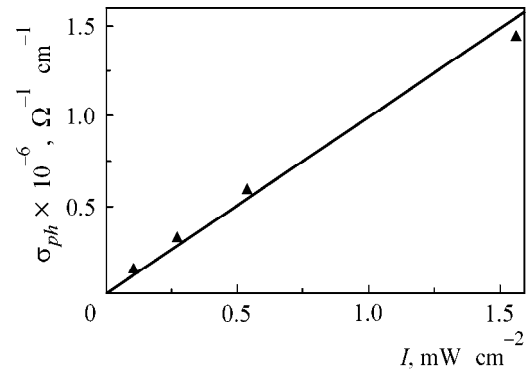
Fig. 4. The linear dependence of the photoconductivity σ_{ph} on the light intensity in PZT; $\lambda \cong 368$ mm.

with [9, 10], we used the following measurement sequence. We applied the external voltage $V = 1$, 3, or 9 V to the electrodes for 100 s with simultaneous illumination of the film by the band-gap light $\lambda \cong 368$ nm. The external electric field was less than the coercive field [9, 10]. After switching off the external field and illumination, the photoinduced hysteresis loop was measured. Then the hysteresis loop was restored by the band-gap illumination in the external low-frequency voltage $\cong 80$ V. The measurement of q was performed for different band-gap light intensities I.

Figure 3 shows the experimental dependence of q on the light intensity I for different values of V. The saturation of the curves in Fig. 3 at $q \ll 1$ and the deviation of the experimental curves from the theoretical dependence $|\ln q| = aI^{-3}$ obtained for two-dimensional domain growth may be connected with many factors. The main possible cause of this deviation is the dependence of the domain-wall velocity v on the screening; the velocity v in Eq. (9) is a function of light intensity I, and $v = v(I)$ decreases with I. A more common reason for this deviation is the infinite-grain approximation that was used in Eq. (3). In any case, Eq. (8) describes the main feature of the phenomenon: an increase in photoinduced hysteresis suppression with light intensity.

The dependence of the domain-wall velocity v on the electric field follows from the behavior of the experimental curves in Fig. 3 at small values of I. It is seen from Eqs. (5) and (9) that $dq/dI \sim qv^dI^{-(d+2)}$ and, therefore, at the initial part $q = q(I)$ (far from saturation) the initial value of dq/dI increases with voltage V. The curves in Fig. 3 confirm this conclusion.

The proposed mechanism of photoinduced hysteresis suppression is fulfilled under the condition

$$\tau_m \leq t_1, \qquad (10)$$

where $t_1 = t_1(E)$ is the effective time of switching polarization; E is the external electric field; and τ_m is the

Maxwellian relaxation time

$$\tau_m = \frac{\varepsilon}{4\pi(\sigma_{ph} + \sigma_d)}, \qquad (11)$$

where σ_{ph} and σ_d are the photoconductivity and dark conductivity, respectively. The dependence of the photoconductivity of the investigated PZT films is shown in Fig. 4 ($\lambda \cong 368$ nm). It shows that in the interval $I \cong 10^{-1}$–0.5 mW cm^{-2} the photoconductivity $\sigma_{ph} = 10^{-7}$–10^{-6} Ω^{-1} cm^{-1} ($\sigma_{ph} \gg \sigma_d$). Therefore, for $\varepsilon \cong 10^3$–10^4, the relaxation time $\tau_m = 10^{-1}$–10^{-3} s.

The time $t_1 = t_1(E)$ depends on the external electric field E. The values of $E \leq 3 \times 10^4$ V cm^{-1} used are much smaller than the coercive field in PZT films $E_c \geq 10^5$ V cm^{-1} [16]. Therefore, t_1 is much larger than the real switching time $t_1 \gg t_{SW}$. We can suppose, therefore, that condition (10) is fulfilled. Nevertheless, the value of q depends on the external electric field E. At small values of the field, $t_1 \gg \tau_m$ but the domain structure change is very small. At high values of the field, $t_1 \leq \tau_m$ and the screening is not effective. It explains the nonmonotonic behavior of the saturation values of $q = q(V)$ in Fig. 3.

Thus, photoinduced hysteresis suppression in ferroelectric PZT films may be explained as a result of the screening of the domain walls by the photocarriers. The YT infinite-grain model switching kinetics permits one to explain the increase in this effect with light intensity. The description of the kinetics of this effect must take into account the dependence of the domain-wall velocity and nucleation rate on the concentration of the photocarriers. It does not mean that the screening of the domain walls is a common mechanism of the PD effect in ferroelectrics.

REFERENCES

1. V. M. Fridkin, *Ferroelectric Semiconductors* (Nauka, Moscow, 1976; Consultants Bureau, New York, 1980).

2. V. M. Fridkin and I. I. Groshik, Appl. Phys. Lett. **10**, 354 (1967).

3. B. P. Grigas, Fiz. Tverd. Tela (Leningrad) **13**, 614 (1971) [Sov. Phys. Solid State **13**, 501 (1971)].

4. V. M. Rudyak and A. A. Bogomolov, Fiz. Tverd. Tela (Leningrad) **9**, 3336 (1967) [Sov. Phys. Solid State **9**, 2624 (1967)].

5. V. P. Bender and V. M. Fridkin, Fiz. Tverd. Tela (Leningrad) **13**, 614 (1971) [Sov. Phys. Solid State **13**, 501 (1971)].

6. V. M. Fridkin, A. A. Grekov, N. A. Kosonogov, *et al.*, Ferroelectrics **4**, 169 (1972).

7. C. E. Land and W. D. Smith, Appl. Phys. Lett. **23**, 57 (1973).

8. C. E. Land and P. S. Peercy, Ferroelectrics **45**, 25 (1982).

9. D. Dimos, W. L. Warren, M. B. Sinclair, *et al.*, Appl. Phys. **76**, 4305 (1994).

10. W. L. Warren and D. Dimos, Appl. Phys. Lett. **64**, 866 (1994).

11. Y. Yshibashi and Y. Takagi, J. Phys. Soc. Jpn. **31**, 506 (1971).

12. K. Dimmler, M. Parris, D. Butler, *et al.*, J. Appl. Phys. **61**, 5467 (1987).

13. H. M. Duiker, P. D. Beale, J. F. Scott, *et al.*, J. Appl. Phys. **68**, 5783 (1990).

14. W. L. Warren, D. Dimos, B. A. Tuttle, *et al.*, Appl. Phys. Lett. **65**, 1018 (1994).

15. L. M. Sheppard, Ceram. Bull. **71**, 85 (1992).

16. S. K. Dey and R. Zuleeg, Ferroelectrics **108**, 37 (1990).

=== **CONDENSED MATTER** ===

Bistable Charge States in a Photoexcited Quasi-Two-Dimensional Electron–Hole System

O. V. Volkov*, I. V. Kukushkin*, D. V. Kulakovskiĭ*, K. von Klitzing**, and K. Eberl**

* Institute of Solid-State Physics, Russian Academy of Sciences, Chernogolovka, Moscow region, 142432 Russia
e-mail: volkov@issp.ac.ru
** Max-Planck Institut für Festkörperforshung, 70569 Stuttgart, Germany
Received March 10, 2000

The luminescence spectra of GaAs/AlGaAs quantum wells (QWs) with low-density quasi-two-dimensional electron and hole channels were studied. It was demonstrated that, at temperatures below some critical value ($T_c \sim 30$ K) and for an excitation power lying in a certain temperature-dependent range, two metastable charge states with two-dimensional charge densities differing in both magnitude and sign can occur in the system under the same conditions. The obtained experimental data agree well with the mathematical model allowing for the transfer of photoexcited carriers to the barrier followed by their tunneling into QW. © 2000 MAIK "Nauka/Interperiodica".

PACS numbers: 73.20.Dx; 33.50.Dq; 78.66.-w

1. Quantum wells (QWs) GaAs/AlGaAs with low-density quasi-two-dimensional (2D) electron and hole channels under photoexcitation are of interest because they allow one to trace the carrier concentration transition from the Fermi system of interacting particles to a system of noninteracting exciton complexes (trions) localized in the Coulomb field of distant impurities [1]. To change the concentration in such systems, one ordinarily uses additional illumination by photons with energy higher than the band gap of the barrier material (AlGaAs) [2]. In this work, we have found that under-barrier excitation (with photon energy lower than the band gap of AlGaAs but higher than that of GaAs) can induce not only dramatic changes in the carrier concentration in QW but also a change in the carrier sign. Moreover, two metastable charge states exhibiting hysteretic behavior upon changing the excitation power can occur in a certain range of temperatures and photoexcitation power densities. We have shown that this phenomenon is of a fundamental nature and is associated with the photoinduced charge transfer in the barrier.

2. We investigated an undoped GaAs QW with $Al_{0.3}Ga_{0.7}As$ barriers grown by molecular-beam epitaxy on an undoped GaAs substrate according to the following scheme: a 1000-Å-wide GaAs buffer layer; an undoped GaAs–AlGaAs superlattice (30 Å–100 Å) with a total thickness of 10 400 Å; a 300-Å AlGaAs barrier; a 200-Å GaAs QW; a 900-Å AlGaAs barrier; and a 100-Å GaAs protective layer. The system was photoexcited by a Ti : sapphire laser with photon energy of 1.61 eV through an optical window in a cryostat or through an 0.8-mm-diameter waveguide. A Ramanor U-1000 double monochromator was used as a spectral instrument, which, in conjunction with a

semiconductor charge-coupled detector, provided a resolution of 0.03 meV. Measurements were made over the temperature range 1.5–40 K.

3. Figure 1a shows the luminescence spectrum measured at a temperature of 3 K and an excitation power density of 50 mW/cm². It consists of two major lines corresponding to the free exciton (X) and the exciton complex (trion). The Zeeman-splitting [2] and zero-magnetic-field optical-orientation (see below) studies allowed the second line to be unambiguously assigned to the emission of a negatively charged exciton complex (X–). This implies that the QW contains a low-density ($\sim 10^{10}$ cm⁻²) 2D electronic system due to electron tunneling into the QW from the residual donor impurities in the barrier. It turned out that the spectrum shape, although independent of the excitation power over a wide range, changed jumpwise upon an increase in the excitation power density above 270 mW/cm²; the changes persisted upon the subsequent decrease in the excitation power back to its initial level. The spectrum measured under the same conditions as the spectrum in Fig. 1a, although for this new metastable state of the system, is shown in Fig. 1b. To establish the cause of such a dramatic change in the spectrum shape, we used the optical orientation method consisting of measuring the degree of circular polarization of the spectral lines upon excitation by circularly polarized light [2]. The difference in the luminescence spectra measured by this method for two polarizations is shown in Fig. 1 by the dashed lines. The essence of the method is that, due to the strong spin–orbit coupling, the photoexcited holes undergo rapid spin relaxation, so that a detectable degree of spin orientation is retained only for the photoexcited electrons. One can see from Fig. 1a that the
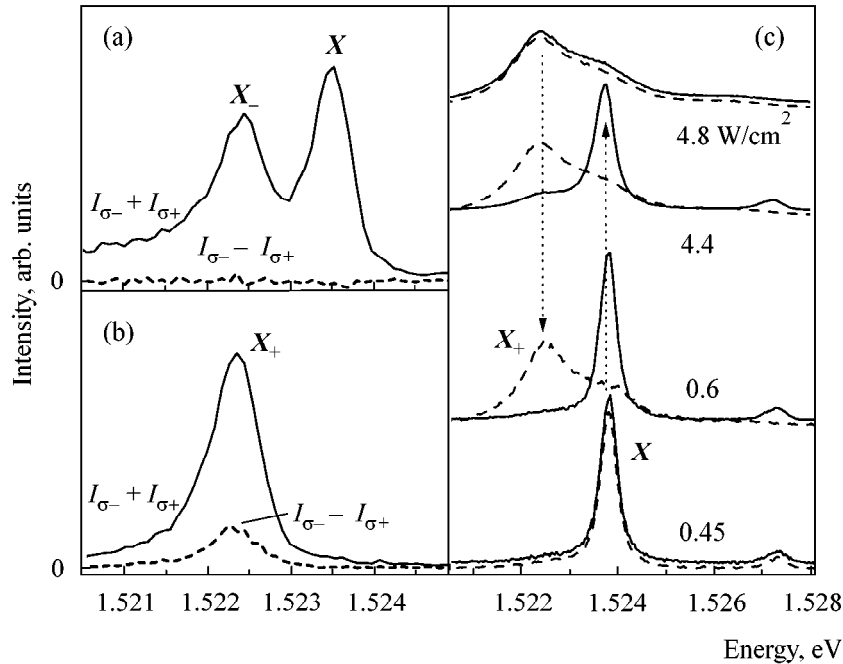
Fig. 1. (a, b) Luminescence spectra (solid lines) and the differences between the spectra measured for two circular polarizations (dashed lines). The spectra are obtained under the same conditions for the two charge states in the bistability region at temperature 3 K. (a) Electronic 2D system obtained upon excitation by light of below-critical intensity. (b) Hole 2D system obtained upon a short-duration increase in the excitation power above the critical value. (c) Normalized luminescence spectra measured at different excitation densities at temperature 17 K. The solid and dashed lines correspond to the spectra measured upon an increase and a decrease in the excitation power, respectively.

$X-$ line is not polarized, because the spins of the two electrons are oppositely aligned in the $X-$ singlet, so that its Zeeman components only differ in the hole spin projections. At the same time, the line observed in the same position in the spectrum of another metastable state is strongly polarized. This signifies that it corresponds to the recombination of a complex containing a single electron, i.e., $X+$. This conclusion is also supported by studying the Zeeman splitting of the $X+$ line in a magnetic field [2]. Therefore, at excitation densities below a certain critical value, the 2D system can exist, depending on the system prehistory, in two different charge states corresponding to the electron and hole channels and realized under the same conditions.

At temperatures below 15 K, the reverse transition from the hole (Fig. 1b) to the electronic (Fig. 1a) state is possible only after switching off the light excitation for a long time (several hours) or upon laser illumination with a photon energy higher than the band gap of AlGaAs. However, the situation changes at $T > 15$ K. The transition from the electronic to the hole state again occurs at a certain excitation power density W_2, while the reverse transition occurs at a power density $W_1 < W_2$. As an example, Fig. 1c displays the luminescence spectra measured at temperature 17 K and different values of excitation density in the regimes of its increase (solid lines) and decrease (dashed lines). One can see that the spec-

trum exhibits hysteretic behavior upon varying the excitation power in the range $W_1 < W < W_2$ (for the indicated temperature, $W_1 = 0.53$ W/cm² and $W_2 = 4.6$ W/cm²). The boundary values W_1 and W_2 of the bistability region depend on the temperature. This dependence (phase diagram) is shown in Fig. 2. The AC curve corresponds to the measured W_2 values; and the BC curve, to the W_1 values. The inset in Fig. 2 demonstrates the method of measuring the W_1 and W_2 values. In the inset, the ratio of the excitonic (X) emission line intensity to the excitation power W is presented as a function of W, measured under the same conditions as the spectra shown in Fig. 1c. Since the increase in the carrier concentration gives rise to screening of the Coulomb interaction and, hence, to exciton dissociation, the I_X/W ratio is closely related to the concentration of the 2D carriers [1]. The range of existence of the bistability manifests itself in the hysteresis of the I_X/W function of W, while the W_1 and W_2 values bound the hysteresis loop upon a decrease and an increase in W, respectively (see Fig. 2). The bistability range narrows upon a further increase in temperature. At the critical point C corresponding to the temperature $T_c = 33$ K, the bistability disappears. At $T > T_c$, the spectrum and, hence, the concentration of 2D carriers, smoothly change with the photoexcitation power.
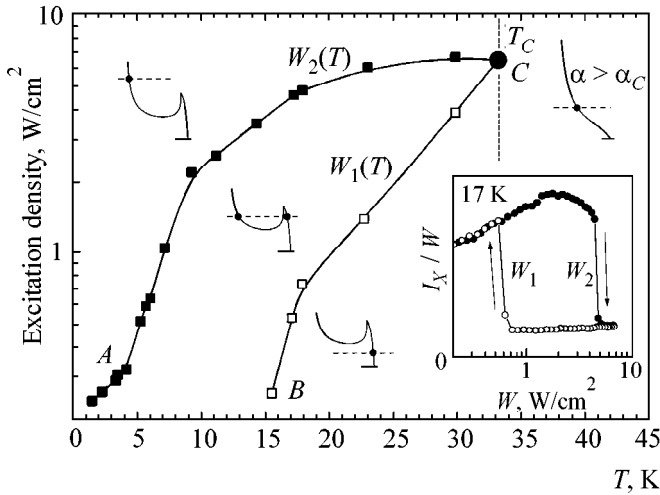
Fig. 2. Phase diagram. The bistability region is bounded by the *ACB* curve, on which the transitions between the charge states occur. The dependence of photocurrent on the concentration of 2D carriers in the QW and the corresponding photocurrent values (dashed lines) in different regions of phase diagram are also shown. The ratio of the exciton (X) emission line intensity to the excitation power W, measured as a function of W at temperature 17 K, is shown in the inset. The W_1 and W_2 values bound the hysteresis range upon a decrease and an increase in W, respectively.

4. The observed changes in the concentration of 2D carriers upon photoexcitation can be caused solely by their redistribution in the sample. We checked experimentally that, upon illumination of the whole sample area, the transitions between the charge states occur uniformly over the whole surface of the sample. This suggests that a change in the carrier concentration in

the QW is caused by charge redistribution among the QW and the barrier. Let us consider a typical structure of a QW with the 2D electron channel and the adjacent barrier (Fig. 3a; for simplicity, only the conduction band profile is shown). The quantum well shown at the left of Fig. 3a contains the 2D electron-density channel n_e formed by virtue of the carriers transferred from the donors distributed with density N_d in the barrier. One can see from Fig. 3a that the electrons in the barrier conduction band are driven by the electric field arising from the charge redistribution, thus creating the current $j = en\mu\mathcal{E}$, where n is the electron concentration, μ is the electron mobility, and $\mathcal{E}$ is the electric field. One can propose several mechanisms of carrier transfer from the QW to the barrier upon excitation by photons with energy lower than the band gap of the barrier material. These may be, e.g., electron–hole recombination umklapp processes in the QW or inelastic light scattering by the QW carriers and their transition to the strongly excited state. Leaving aside the question of a particular phototransfer mechanism, we focus on what further happens to the charge carriers. Clearly, the total current $j(0)$ flowing from the QW into the barrier through the well boundary ($x = 0$) must be equal to the current of the reverse carrier tunneling into the well, j_t, integrated across the whole barrier width. It is this condition which determines the steady-state electron concentration n_e in the well. At low temperatures in the absence of photoexcitation, the under-barrier tunneling has an extremely small amplitude, because the electron wave function exponentially decays in the barrier even at distances of several tens of Å. Under these conditions, the electrons transferred into the barrier can be left there for a very long time [3]. In our experiments,
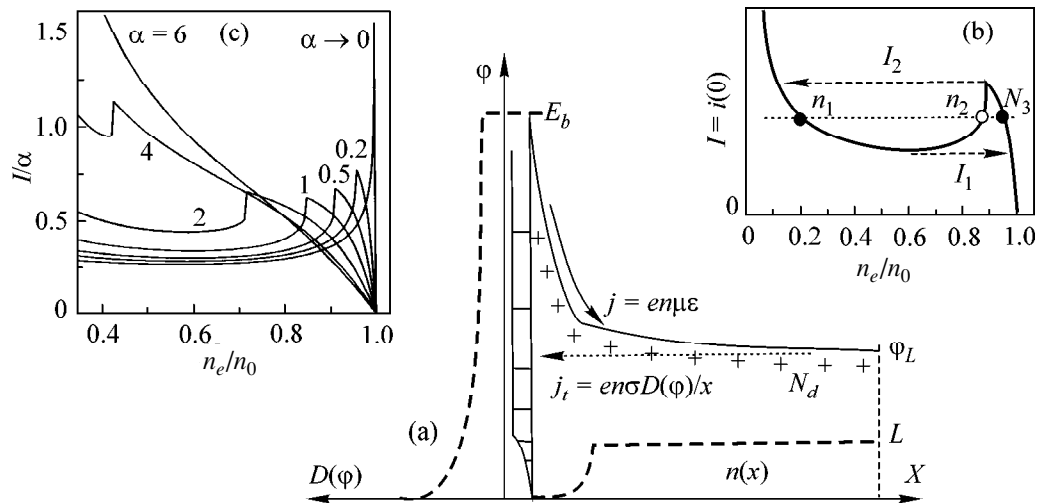
Fig. 3. (a) Schematic representation of current flow in the barrier upon photoexcitation. The photoexcited-carrier current j flowing into the barrier is compensated by the current j_t due to the reverse under-barrier tunneling. The tunnel current is proportional to the effective density $D(\varphi)$ of final states, shown at the left by the dashed line. At the bottom, the dashed line indicates the carrier concentration n in the barrier. (b) The photoexcited-carrier current as a function of the concentration of 2D electrons in the QW, calculated for $\alpha = 0.7$. (c) The dimensionless photoexcited-carrier current normalized to α vs. the concentration of 2D carriers in the QW, calculated for different α values.

this results in long relaxation times of transition from the hole to the electronic state at low (< 15 K) temperatures in the absence of photoexcitation. At the same time, it is known that thermodynamic equilibrium in the sample under light excitation is established in times on the order of a fraction of a second [4]. The time of the photoinduced switching from the electronic to the hole state turned out to be of the same order. In this case, a different tunneling mechanism becomes operative, viz., a hopping conduction through the in-gap impurity states. Both the accidental dopant atoms (Si) in AlGaAs and the configuration defects [5] that are invariably present in the alloy can serve as impurities. The excited impurity states with large-radius wave functions are the most active in the tunneling process. Because of this, the tunnel current increases with the excitation power or the temperature [6]. As the barrier width increases, the tunnel current decreases in inverse proportion to the width because of a mere increase in the number of impurities involved in the process. In addition, the tunnel current is proportional to the density of final states in the QW, i.e., to the density of size-quantization subbands. Inasmuch as the subband energies in a well of width W with infinitely high walls are equal to $\varphi_n = E_0 n^2$, where $E_0 = (\pi\hbar/W)^2/2m$, the density-of-final-state factor can be represented in the dimensionless form as $D(\varphi_n) = \varphi_0/(\varphi_{n+1} - \varphi_n)$, i.e., $D(\varphi) = (2\sqrt{\varphi/E_0} + 1)^{-1}$. Therefore, the tunnel current per unit barrier width can be represented as $j_t = en\sigma D(\varphi)/x$, where σ is the barrier "penetrability" dependent on the excitation power and the temperature. The j, $\mathscr{E}$, and φ quantities are related to each other by the following equations: $j' = -j_t$; $\mathscr{E}' = -4\pi e(N_d - n)$; and $\varphi' = -\mathscr{E}$. The boundary conditions have the form $j(0) = J$; $\mathscr{E}(0) = 4\pi en_e$; $\varphi(0) = E_b$; and $\mathscr{E}(L) = 0$, where E_b is the potential barrier height for the carriers, J is the total current of photoexcited particles, and L is the barrier width (Fig. 3a). Let us pass to the dimensionless quantities by substituting $x/L \longrightarrow x$; $j \cdot L/(e\mu E_b N_d) \longrightarrow i$; $\mathscr{E}L/E_b \longrightarrow e$; and $\varphi/E_b \longrightarrow \varphi$ and introducing the dimensionless parameters $\alpha = \sigma L/\mu E_b$; $\beta = N_d L/n_x$; and $\gamma = E_b/E_0$, where $n_x = E_b/4\pi eL$. The set of equations in the dimensionless variables has the form

$$i' = -\frac{\alpha}{x}\frac{i}{e}f(\varphi), \quad e' = -\beta\left(1 - \frac{i}{e}\right), \quad \varphi' = -e, \quad (1)$$

where $f(\varphi) = (2\sqrt{\gamma\varphi} + 1)^{-1}$ if $\varphi \geq 0$ and $f(\varphi) = 0$ if $\varphi < 0$. The boundary conditions are $i(0) = I$; $e(0) = n_e/n_x$; $\varphi(0) = 1$; and $e(1) = 0$. The system of Eqs. (1) has a physically meaningful solution at $0 < n_e \leq n_0$, where $n_0 = n_x\sqrt{2\beta}$ is the equilibrium concentration in the absence of illumination, when $n_e = n_0$, $I = 0$, and $\varphi(1) = 0$. Hereafter, the barrier is assumed to be "wide," such that $\beta > 2$. The solutions at $n_e < n_0$ correspond to the nonzero photocurrent $I > 0$ and can only be numerically

obtained. We have solved the system of Eqs. (1) with a set of parameters close to those of the examined sample: $W = 200$ Å, $L = 10\,000$ Å, $N_d = 6 \times 10^{14}$ cm^{-3}, and $E_b = 250$ MeV, so that $n_0 = 1.3 \times 10^{10}$ cm^{-2}, $\beta = 43.4$, and $\gamma = 17.9$. The result for $\alpha = 0.7$ is shown in Fig. 3a. One can distinguish between two domains in the potential profile shown in Fig. 3a for $n_e = 0.71n_0$. In the first one, $0 < x < n_e/N_d$, the carrier density (shown by the dashed curve at the bottom) is small. In the second domain, $n_e/N_d < x < L$, it is close to N_d, and $\mathscr{E} \approx 0$ and $\varphi \approx \varphi_L = $ const. Since the tunnel current mainly flows from the second domain, the $I(n_e)$ dependence is primarily determined by the density-of-states factor $D(\varphi_L)$ (shown by the dashed line at the left in Fig. 3a). This gives rise to a peak in the $I(n_e)$ dependence in the vicinity of n_0 (Fig. 3b). The resulting ascending portion of the $I(n_e)$ curve forms the bistability region. If the excitation power density is such that $I_1 < I < I_2$, the system can occur in three different charge states $n_1 < n_2 < n_3$ (Fig. 3b), with only n_1 and n_3 being stable. The $I(n_e)$ dependence is primarily governed by the α parameter. As it increases, the stepped $n(x)$ profile is blurred, resulting in the disappearance of the bistability region in the $I(n_e)$ dependence at $\alpha > \alpha_c \approx 5$. The set of solutions $I(n_e)$ obtained for different α values is presented in Fig. 3c. Conversely, a decrease in α brings about peak sharpening. In the $\alpha \longrightarrow 0$ limit, one arrives at a θ-function-like $n(x)$ profile and a solution of the form $I(n_e) = \alpha\ln((\beta/2)^{1/2}(n_0/n))/(2(\gamma(1 - n^2/n_0^2))^{1/2} + 1)$. A change in the β parameter weakly affects the $I(n_e)$ dependence, while the γ parameter determines the peak height and, correspondingly, the bistability range.

A comparison of the model described above with our experimental results brings up two questions. First, it was found that not only the carrier concentrations but also the carrier signs changed in the experiment. A plausible explanation may be that the QW is confined by two barriers grown using different technologies. For simplicity, we omitted from consideration the barrier grown over the QW, because it is more than an order of magnitude thinner than the barrier on the substrate side. However, the impurities in this barrier create an additional carrier concentration (which may even be of the opposite sign) in the well, thereby shifting the $I(n_e)$ curve along the n_e-axis. Second, the calculated range of $I(n_e)$ bistability (I_2/I_1 in Fig. 3b) is tangibly narrower than the experimentally observed W_2/W_1 ratio (Fig. 2) up to a temperature of 25 K, while at temperatures lower than 15 K W_1, it defies measurement at all. The reason is that the decrease in the excitation power gives rise not only to a linear decrease in the photoinduced current I but also to a decrease in the barrier penetrability σ. Insofar as the hopping conductivity through the impurities in the barrier has a photo- and thermally activated nature, σ and, hence, α also linearly depend on the excitation power W over a certain range. For this

reason, one can escape the I/α bistability region (Fig. 3c) only upon saturation of the linear $\sigma(W)$ dependence. The lower limit $\sigma(W)$ for the saturation corresponds to the barrier penetrability in the absence of photoexcitation. At low temperatures, this quantity is exceedingly small, while the characteristic times for establishing equilibrium in the system are long. This renders the W_1 value practically unmeasurable in a reasonable time. At the same time, the barrier dark penetrability increases with temperature and the linear portion of the $\sigma(W)$ curve narrows. With a rise in temperature, the σ value increases by itself at a fixed excitation power, resulting in an increase in W_1 and W_2 (Fig. 2). The α parameter also increases in proportion to σ. This is accompanied by the narrowing of the bistability range at a fixed excitation power; and the bistability fully disappears at $\alpha = \alpha_c$, which corresponds to the C point in the phase diagram (Fig. 2). To illustrate the interrelation between the phase diagram and the form of the $I(n_e)$ dependence, the corresponding $I(n_e)$ functions are shown in Fig. 2 in different regions of the phase plane and the I values are denoted by the dashed lines. Curiously, the resulting phase diagram resembles the liquid–gas phase diagram, while the $I(n_e)$ dependence resembles the Van der Waals isotherm.

REFERENCES

1. O. V. Volkov, V. E. Zhitomirskiĭ, I. V. Kukushkin, *et al.*, Pis'ma Zh. Éksp. Teor. Fiz. **66**, 730 (1997) [JETP Lett. **66**, 766 (1997)].

2. O. V. Volkov, V. E. Zhitomirskiĭ, I. V. Kukushkin, *et al.*, Pis'ma Zh. Éksp. Teor. Fiz. **67**, 707 (1998) [JETP Lett. **67**, 744 (1998)].

3. M. I. Nathan, Solid-State Electron. **29**, 167 (1986).

4. I. V. Kukushkin, K. V. Klitzing, K. Ploog, *et al.*, Phys. Rev. B **40**, 4179 (1989).

5. C. V. Reddy, Y. L. Luo, S. Fung, and C. D. Beling, Phys. Rev. B **58**, 1358 (1998).

6. A. L. Efros and B. L. Shklovskiĭ, *Electronic Properties of Doped Semiconductors* (Nauka, Moscow, 1979; Springer-Verlag, New York, 1984).

Translated by V. Sakun

================ **CONDENSED MATTER** ================

Theory of Vortex Lattice Effects on STM Spectra in *d*-Wave Superconductors[1]

A. S. Mel'nikov

Institute of Physics of Microstructures, Russian Academy of Sciences, Nizhni Novgorod, 603600 Russia
e-mail: melnikov@ipm.sci-nnov.ru
Received March 20, 2000

The theory of scanning tunneling spectroscopy of low-energy quasiparticle (QP) states in vortex lattices of *d*-wave superconductors is developed taking account of the effects caused by an extremely large extension of QP wavefunctions in the nodal directions and the band structure in the QP spectrum. The oscillatory structures in STM spectra, which correspond to van Hove singularities, are analyzed. Theoretical calculations carried out for finite temperatures and scattering rates are compared with recent experimental data for high-T_c cuprates. © 2000 MAIK "Nauka/Interperiodica".

PACS numbers: 74.20.-z; 74.25.Jb; 74.60.-w; 74.72.-h

The electronic structure of the mixed state in *d*-wave superconductors reveals a number of fundamentally new features (see [1–9] and references therein), as compared to the case of *s*-wave compounds, where low-lying quasiparticle (QP) states are bound to the vortex core and weakly perturbed by the presence of neighboring vortices at magnetic fields $H \ll H_{c2}$. The vanishing pair potential in the nodal directions results in the extremely large extension of QP wavefunctions, which are sensitive to the superfluid velocity ($\mathbf{V}_s$) fields of all vortices; and, thus, the electronic structure is influenced by the vortex lattice geometry. The resulting peculiarities of the local density of states (DOS) can be detected, e.g., by a scanning tunneling microscope (STM). In this paper, we focus on the theory of scanning tunneling spectroscopy of low-energy QP states in vortex lattices of *d*-wave superconductors and compare the theoretical calculations with recent experimental data [10, 11] for high-T_c cuprates, where the dominating order parameter is believed to be of *d*-wave symmetry. Hereafter, we assume the Fermi surface (FS) to be two-dimensional (2D) and take the gap function in the form $\Delta_{\mathbf{k}} = 2\Delta_0 k_x k_y / k_F^2$ (the *x*-axis makes an angle of $\pi/4$ with the *a* axis of the CuO_2 planes). Let us orient **H** along the *c* axis ($H_{c1} \ll H \ll H_{c2}$) and consider two types of vortex lattices: (I) rectangular lattice with primitive translations $\mathbf{a}_1 = a\mathbf{x}_0$ and $\mathbf{a}_2 = \sigma a\mathbf{y}_0$ and (II) centered rectangular lattice with $\mathbf{a}_1 = a\mathbf{x}_0$ and $\mathbf{a}_2 = a(\mathbf{x}_0/2 - \sigma\mathbf{y}_0)$, where $H\sigma a^2 = \phi_0$ is the flux quantum and $\mathbf{x}_0$, $\mathbf{y}_0$, and $\mathbf{z}_0$ are the unit vectors of the coordinate system.

Van Hove singularities. Our consideration is based on the analysis of the Bogolubov–de Gennes (BdG) equations for low-energy excitations with momenta

close to a certain gap node direction (e.g., $\mathbf{k}_1 = k_F\mathbf{x}_0$): $(\hat{H}_0 + \hat{H}')\hat{g} = \varepsilon\hat{g}$, where $\hat{g} = (u, v)$ is the QP wavefunction; $\hat{H}_0 = V_F\hat{\sigma}_z\hat{p}_x + V_\Delta\hat{\sigma}_x\hat{p}_y$; $\hat{\sigma}_x$ and $\hat{\sigma}_z$ are the Pauli matrices; $\hat{H}' = MV_FV_{sx}(1 + \hat{\sigma}_z) + MV_\Delta V_{sy}\hat{\sigma}_x$; M is the electron effective mass; $\hat{\mathbf{p}} = -i\hbar\nabla - e\mathbf{A}/c$; $V_F = \hbar k_F/M$; $V_\Delta = 2\Delta_0/(\hbar k_F)$; $\mathbf{H} = -H\mathbf{z}_0$; $\mathbf{A} = Hy\mathbf{x}_0$; and $\mathbf{V}_s = (V_{sx}, V_{sy})$. The spectrum of the Dirac Hamiltonian $\hat{H}_0$ can be obtained using the usual quantization rule for a cyclotron orbit (CO) area [4, 5]. The periodic potential $\hat{H}'$ removes the degeneracy of the discrete energy levels with respect to the CO center and induces a band structure in the spectrum [3, 6–8]. The general solution can be written in the form of a magnetic Bloch wave:

$$\hat{g} = \sum_n \exp\{ix(q_x + 2\pi n/a) + 2in\sigma q_y a\} \times \hat{G}(y - 2n\sigma a, \mathbf{q}), \tag{1}$$

where *n* is an integer and **q** is the quasi-momentum lying within the first magnetic Brillouin zone (MBZ): $-\pi/(2a) < q_x < \pi/(2a)$, $-\pi/(2\sigma a) < q_y < \pi/(2\sigma a)$. The wavefunction $\hat{G}(y, \mathbf{q})$ is localized in the domain with the size *L* determined by *q* and energy values. The potential $\hat{H}'$ results in the splitting of the CO near the MBZ boundaries (see Fig. 1), and the spectrum consists of branches which correspond to the split portions of the CO. For large Dirac cone anisotropy $\alpha = V_F/V_\Delta \gg 1$ ($\alpha = k_F\xi_0/2$) and $\varepsilon < 0.5\varepsilon^*$ ($\varepsilon^* = \pi\hbar V_F/a \sim \Delta_0\sqrt{H/H_{c2}}$), the harmonics in Eq. (1) do not overlap ($L < 2\sigma a$) and one can replace $\hat{H}'$ by the potential $\langle\hat{H}'\rangle_x$ averaged in

---

[1] This article was submitted by the author in English.
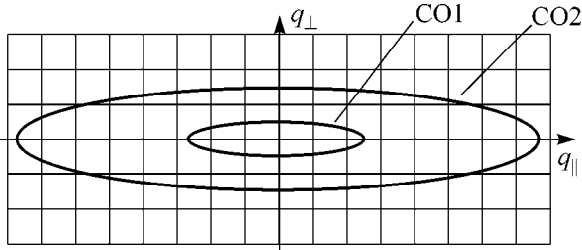
Fig. 1. Cyclotron orbits (CO1, CO2) and MBZ boundaries for a square lattice. ($q_\parallel$, $q_\perp$) defines a coordinate system whose origin is at the node, with $q_\perp$ ($q_\parallel$) normal (tangential) to the FS.

Fig. 2. Energy branches for (a) $\pi\sigma\alpha = 50$ and (b) $\pi\sigma\alpha = 100$.

the x direction (see [3]). Such a simplification is a natural consequence of the small size of the cyclotron orbit (CO1 in Fig. 1) in the nodal direction, as compared to the size of the MBZ. The energy spectrum consists of branches $\varepsilon_n(q_x = \pi Q/a) = \varepsilon^* E_n(Q, \sigma\alpha)$, which are displayed in Fig. 2 in the first MBZ for $\pi\sigma\alpha = 50$ and $\pi\sigma\alpha = 100$. The number of energy branches which cross the Fermi level can be determined as follows: $N \sim 2q_\parallel^* / \delta q_\parallel \sim 2\sqrt{\pi\sigma\alpha}$, where $q_\parallel^*$ is the minimum possible size of the CO in the $q_\parallel$ direction and $\delta q_\parallel$ is the distance between MBZ boundaries. Each energy branch has an extremum as a function of the momentum q_x near the MBZ boundary at a certain $\tilde{\varepsilon}_n$ (here we neglect additional extrema which appear due to the exponentially small splitting of energy levels near the points of intersection of the branches in the E–Q plane). Due to the one-dimensional (1D) nature of the low-energy spectrum, the divergent contributions to the DOS take the form $\delta N(\varepsilon) \sim |\varepsilon - \tilde{\varepsilon}_n|^{-1/2}$ ($\varepsilon > \tilde{\varepsilon}_n$ for energy minima and $\varepsilon < \tilde{\varepsilon}_n$ for maxima). The distance between these peaks $\delta\varepsilon \sim \varepsilon^*/(2\sigma\alpha)$ coincides with a characteristic energy scale corresponding to the van Hove singularities, which occur when the CO intersects MBZ boundaries in the q_y direction (see Fig. 1). The crossover between 1D and 2D regimes in the band spectrum occurs at $\varepsilon_c \sim 0.5\varepsilon^*$, when the CO size in the $q_\perp$ direction becomes larger than the size of the first MBZ (CO2 in Fig. 1). For $\varepsilon \gtrsim \varepsilon_c$, the q_y-dependence of energy becomes essential and results in the appearance of 2D critical points, i.e., 2D local maxima (or minima) and saddle points. Thus, instead of square-root van Hove singularities, we obtain a set of discontinuities and logarithmic features ($\delta N(\varepsilon) \sim -\ln|1 - \varepsilon/\tilde{\varepsilon}_n|$) in the DOS, respectively. Obviously, these 2D singularities are more sensitive to temperature and finite-lifetime effects and, consequently, the suppression of the corresponding oscillatory structure in the DOS should be stronger in the high-energy regime. The above analysis can be generalized for gap nodes at $\mathbf{k} = \pm k_F \mathbf{y}_0$; the corresponding energy scales take the form $\delta\varepsilon \sim 0.5\varepsilon^*/\alpha$ and $\varepsilon_c \sim 0.5\varepsilon^*/\sigma$.
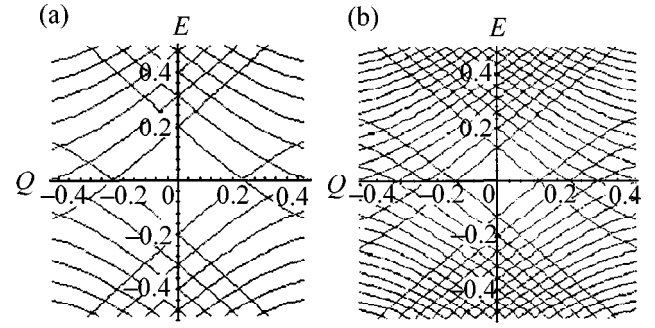
Even in the low-energy regime, the DOS oscillations with the energy scale $\delta\varepsilon$ are surely smeared due to a finite scattering rate Γ and temperature and can be observed only for a moderate Dirac cone anisotropy and rather large magnetic fields. Comparing our results with a numerical solution [7] of the BdG equations for $\sigma = 1$ and $\alpha = 5/2$, we find that the above mechanism gives a good estimate of the energy scale of the double-peak structure in the tunneling conductance at the core center at $H/H_{c2} = 0.3$ ($\delta\varepsilon \sim 0.1\Delta_0$) and can explain the absence of this structure at low fields $H/H_{c2} = 0.05$ by temperature broadening ($T = 0.1T_c > \delta\varepsilon \sim 0.05\Delta_0$). In principle, the van Hove singularities may account for peaks with the large energy gap $\sim\Delta_0/4$ observed experimentally at the vortex centers in YBaCuO [10] at $H \approx 6$ T, provided we assume $\alpha \sim 1$. Unfortunately, the latter assumption is not consistent with the results of thermal conductivity measurements [12] ($\alpha \sim 14$); and, thus, the nature of the experimentally observed peaks is still unclear. It is also necessary to stress here that the critical points in the DOS are a direct consequence of perfect periodicity, so that the introduction of rather strong disorder surely removes these singularities.

Zero-bias conductance. Hereafter, we neglect the DOS oscillations discussed above and consider the peculiarities of the zero-bias tunneling conductance $g(\mathbf{r})$ starting with a modified semiclassical model proposed in [3]. According to this approach, the Doppler shift of the QP energy, which plays an important role for $\varepsilon \lesssim \Delta_0\sqrt{H/H_{c2}}$, appears to be averaged in the nodal direction due to the extremely large size of a semiclassical wave packet in this energy interval. Within such an approximation, a diagonal (retarded) Green function can be written in the form

$$G^R(\mathbf{k}, \varepsilon, \mathbf{r}) = \frac{\varepsilon + i\Gamma - \hbar\mathbf{k}_F\mathbf{V}_{av} + \epsilon_\mathbf{k}}{(\varepsilon + i\Gamma - \hbar\mathbf{k}_F\mathbf{V}_{av})^2 - \Delta_\mathbf{k}^2 - \epsilon_\mathbf{k}^2}, \quad (2)$$

where $\epsilon_\mathbf{k}$ is the normal-state electron dispersion and $\mathbf{V}_{av} = \langle\mathbf{V}_s\rangle_x + \langle\mathbf{V}_s\rangle_y$. The scattering rate Γ should be determined self-consistently: $\Gamma = N(\Gamma, \varepsilon)/2N_F\tau$ (Born limit) and $\Gamma = N_F\Gamma_u/N(\Gamma, \varepsilon)$ (unitary limit), where 2τ and N_F are the relaxation time and DOS at the Fermi level in the nor-
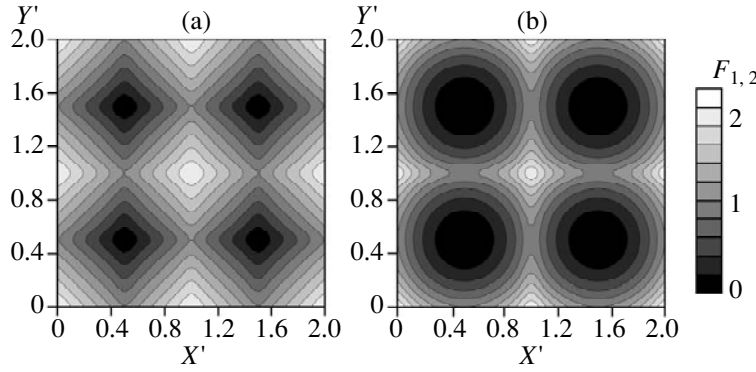
Fig. 3. Contour plots of the functions (a) F_1 and (b) F_2, which determine the spatial variation of the zero-bias tunneling conductance for a square lattice ($x' = x/a$, $y' = y/a$).

mal state; $\Gamma_u = n_{imp}/\pi N_F$; n_{imp} is the concentration of point potential scatterers; and $N(\Gamma, \varepsilon) = -\mathrm{Im}\int G^R d^2k/(2\pi^3)$ is the local DOS. Let us first consider the effect of finite temperature on the zero-bias conductance in the clean limit ($\Gamma \longrightarrow 0$). The expression for the normalized conductance reads

$$\tilde{g}(\mathbf{r}) = \frac{g(\mathbf{r})}{g_N} = \int_{-\infty}^{+\infty} \frac{N(\Gamma = 0, \varepsilon)d\varepsilon}{4 N_F T \cosh^2(\varepsilon/2T)}$$
$$= \frac{T\ln 2}{\Delta_0} + \frac{T}{2\Delta_0} \sum_{i = x, y} \ln \cosh \frac{\varepsilon_i^* \Phi_i}{4T}. \quad (3)$$

Here, g_N is the normal-state conductance, $\Phi_x = \Phi(x/R_x)$, $\Phi_y = \Phi(y/R_y)$, $\Phi(z) = 2z - (2m + 1)$ for $m < z < m + 1$ (m is an integer), R_y (R_x) is the distance between the lines parallel to the $x(y)$-axis and passing through the vortex centers, $\varepsilon_x^* = \pi\hbar V_F H R_x/\phi_0$, and $\varepsilon_y^* = \pi\hbar V_F \sigma/R_y$. For type I (II) lattices we have $R_x = a$ and $R_y = \sigma a$ ($R_x = a/2$, $R_y = \sigma a$). One can separate two qualitatively different regimes in the behavior of the conductance:

(i) Superflow-dominated regime $T \ll \varepsilon_{x, y}^*$,

$$\tilde{g} \simeq \frac{1}{8}\sqrt{\frac{\pi\sigma H}{2 H_{c2}}} F_1(x, y); \quad (4)$$

(ii) Temperature-dominated regime $T \gg \varepsilon_{x, y}^*$,

$$\bar{g} \simeq \frac{T\ln 2}{\Delta_0} + \frac{\pi\Delta_0\sigma H}{32 T H_{c2}} F_2(x, y), \quad (5)$$

where $F_1(x, y) = |\Phi_x|(R_x/R_y) + |\Phi_y|$ and $F_2(x, y) = \Phi_x^2 (R_x/R_y)^2 + \Phi_y^2$. In Fig. 3, we display the contour plots of the functions $F_1(x, y)$ and $F_2(x, y)$ for a square lattice of type I (which is close to the one observed experimentally in YBaCuO [10]). There are two consequences of an increase in temperature: (i) First, the spatial dimensions of peaks in the local DOS become

rather small, compared to the intervortex distance, only for $T > T^* \sim \Delta_0\sqrt{H/H_{c2}}$. (ii) Second, the amplitude of the peaks proves to be essentially suppressed in the limit $T \gg T^*$. For magnetic fields $H \sim 6\,\mathrm{T}$ (which is typically the field of STM experiments [10, 11]), one obtains $T^* \sim 20\,\mathrm{K}$. Thus, we conclude that the finite-temperature effects can explain neither the narrow zero-bias conductance peaks observed in YBaCuO nor the absence of these peaks in BiSrCaCuO at $T = 4.2\,\mathrm{K}$. To explain these experimental facts, it is necessary to take account of the finite-lifetime effects, which can strongly influence the behavior of the DOS, as follows from the results of [13–15] obtained on the basis of the usual semiclassical approach with a local Doppler shift. Starting with the modified semiclassical model (2), we obtain the following expression for the tunneling conductance at $T = 0$:

$$\tilde{g} = \frac{N(\Gamma, \varepsilon = 0)}{N_F} = \frac{\Gamma}{4\pi\Delta_0}\left(4\ln\frac{\Delta_0}{\Gamma} + \sum_{i = x, y} f_i\right),$$
$$f_i = \frac{\varepsilon_i^*|\Phi_i|}{\Gamma}\tan^{-1}\frac{\varepsilon_i^*|\Phi_i|}{2\Gamma} - \ln\left(1 + \frac{(\varepsilon_i^*\Phi_i)^2}{4\Gamma^2}\right). \quad (6)$$

Obviously, Born scatterers result only in a moderate change in the DOS (see [13]), since the corresponding Γ value for $\Delta_0\tau \gg 1$ is very small compared to $\varepsilon_{x, y}^*$ and the conductance is given by Eq. (4). In contrast, in the unitary limit, Eq. (4) is valid only in the clean case $\Gamma_u \ll \Gamma_{x, y}^* \sim 0.1\varepsilon_{x, y}^2/\Delta_0$ (for a square lattice $\Gamma_{x, y}^* \sim 0.1\Delta_0 H/H_{c2}$). In the dirty limit $\Gamma_u \gg \Gamma_{x, y}^*$, we obtain

$$\tilde{g} \simeq \tilde{g}(H = 0)\left(1 + \frac{\Delta_0 H\sigma}{64\Gamma_u H_{c2}} F_2(x, y)\right), \quad (7)$$

where $\tilde{g}(H = 0) \simeq 0.5\sqrt{\Gamma_u/\Delta_0}$. In the vicinity of each vortex center, the local DOS exhibits a fourfold sym-

metry with maxima along the nodal directions, in good agreement with numerical calculations based on the Eilenberger theory [16]. For $H = 6$ T, the finite-lifetime effects become substantial if we assume $\Gamma_u \gtrsim 10^{-2}\Delta_0$. Thus, our approach allows one to explain the rather narrow conductance peaks (see Fig. 3b) observed near vortex centers in YBaCuO [10], even without taking account of the nontrivial structure of the tunneling matrix element discussed in [15]. With a further increase in the Γ_u value, the amplitude of the peaks at the vortex centers vanishes: $\delta\tilde{g} \sim \sqrt{\Delta_0/\Gamma_u}\,(H/H_{c2})$. Such a high sensitivity of the $\delta\tilde{g}$ value to the finite-lifetime effects can probably explain the difficulties in the observation of these peaks in the mixed state of BiSrCaCuO [11]. Note in conclusion that, according to Eq. (7), the spatially averaged DOS in the dirty limit varies as H rather than $H\ln H$ (the latter dependence was predicted in [13, 14] within the semiclassical approach allowing for the local $\mathbf{V}_s$ value).

REFERENCES

1. G. E. Volovik, Pis'ma Zh. Éksp. Teor. Fiz. **58**, 457 (1993) [JETP Lett. **58**, 469 (1993)].

2. L. P. Gor'kov and J. R. Schrieffer, Phys. Rev. Lett. **80**, 3360 (1998).

3. A. S. Mel'nikov, cond-mat/9806188; J. Phys.: Condens. Matter **11**, 4219 (1999).

4. P. W. Anderson, cond-mat/9812063.

5. B. Jankó, Phys. Rev. Lett. **82**, 4703 (1999).

6. M. Franz and Z. Tešanović, Phys. Rev. Lett. **84**, 554 (2000).

7. K. Yasui and T. Kita, Phys. Rev. Lett. **83**, 4168 (1999).

8. L. Marinelli, B. I. Halperin, and S. H. Simon, cond-mat/0001406.

9. N. B. Kopnin and V. M. Vinokur, cond-mat/0002337.

10. I. Maggio-Aprile, Ch. Renner, A. Erb, *et al.*, Phys. Rev. Lett. **75**, 2754 (1995).

11. Ch. Renner, B. Revaz, K. Kadowaki, *et al.*, Phys. Rev. Lett. **80**, 3606 (1998).

12. M. Chiao, R. W. Hill, C. Lupien, *et al.*, Phys. Rev. Lett. **82**, 2943 (1999).

13. Yu. S. Barash, V. P. Mineev, and A. A. Svidzinsky, Pis'ma Zh. Éksp. Teor. Fiz. **65**, 606 (1997) [JETP Lett. **65**, 638 (1997)].

14. C. Kübert and P. J. Hirschfeld, Solid State Commun. **105**, 459 (1998).

15. M. Franz and Z. Tešanović, Phys. Rev. B **60**, 3581 (1999).

16. M. Ichioka, A. Hasegawa, and K. Machida, Phys. Rev. B **59**, 184 (1999).

===== **CONDENSED MATTER** =====

Photon Hole-Current Drag in Germanium

L. E. Vorob'ev*, D. V. Donetskiĭ**, and D. A. Firsov*

*St. Petersburg State Technical University, ul. Politekhnicheskaya 29, St. Petersburg, 195251 Russia
e-mail: dmfir@twonet.stu.neva.ru
**State University of New York at Stony Brook, New York 11794-3800, USA
Received March 21, 2000

A novel phenomenon of photon hole-current drag in hole semiconductors was observed for the first time. The effect was observed in *p*-Ge and consisted in the appearance of a difference in refractive indices for light propagating along an electric current and in the opposite direction. The effect was observed at a wavelength of 10.6 μm. It can be explained in terms of virtual intersubband transitions of hot holes. © *2000 MAIK "Nauka/Interperiodica".*

PACS numbers: 72.40.+w

According to Onsager's principle of microscopic reversibility, in crystals with an inversion center [1],

$$\epsilon(\boldsymbol{\chi}, \omega) = \epsilon(-\boldsymbol{\chi}, \omega), \qquad (1)$$

where χ is the wavenumber and ω is the light frequency.

Therefore, the expansion of the dielectric constant tensor contains only even powers of χ, so that a change in the direction of light propagation does not change the refractive index. Electric field or current **j** breaks the symmetry of a system, leading to the appearance of linear terms in the expansion of ϵ in powers of χ:

$$\epsilon_{ik}(\boldsymbol{\chi}) = \epsilon_{ik}(0) + B_{iklm}j_l\chi_m. \qquad (2)$$

In other words, the current in a semiconductor gives rise to a current-direction-dependent increment $\Delta\epsilon(\mathbf{j}, \boldsymbol{\chi})$ in the dielectric constant.

A change in the real part of the dielectric constant results in a change in the refractive index, i.e., the light velocity in a crystal. Therefore, an electric current induces a "photon drag."

A light electron drag (current-induced change in the refractive index of a crystal) was observed for *n*-InAs in [2]. The authors of that work attributed this effect to a Fresnel light electron drag, which appears in semiconductors as a result of the relativistic velocity summation in a system where light propagates through a moving medium. The phenomenological theory of Fresnel light drag was developed in [2] with allowance made for the Doppler effect. This drag effect was presented as the first solid-state relativistic effect produced by slowly moving electrons.

The drag effect in electron semiconductors was explored in a number of theoretical works [3–5]. In these works, the results obtained in [2] were explained by the fact that the directed electron motion introduces asymmetry into the process of momentum redistribu-

tion among the electron and photon subsystems. A linear response of an electron gas with an isotropic dispersion law to the perturbation introduced by an electromagnetic wave was considered, and it was shown that this effect arises because of the nonparabolic form of the conduction band. It was theoretically demonstrated in [6] that, owing to the more complicated structure of the valence band, as compared to the conduction band, the photon-drag effect in *p*-type semiconductors may be 4–6 orders of magnitude more pronounced than the electron effect observed in [2]. This result becomes understandable when comparing the effect under discussion with the charge-carrier light drag effect, which is most pronounced in *p*-type semiconductors [7]. Both these phenomena have a common microscopic mechanism of momentum redistribution between the hole and photon subsystems. The use of a simplified theory for obtaining a lower estimate for the magnitude of the effect allowed the following expression to be derived for the linear contribution of current **j** to the real part of the dielectric constant [6]:

$$\Delta\epsilon(\mathbf{j}, \boldsymbol{\chi}) = \frac{4\pi e}{\omega^3 m_0}(\boldsymbol{\chi} \cdot \mathbf{j})\frac{6\gamma}{\gamma_1 - 2\gamma}\left(\frac{14}{5}\gamma + k\right), \qquad (3)$$

where γ, γ_1, and k are the Luttinger parameters of the isotropic approximation and m_0 is the free-electron mass. Since $\Delta\epsilon$ is small, the corresponding change in the refractive index is $\Delta n = \Delta\epsilon/2n$.

Model of the phenomenon. Let us invoke the optical intersubband hole transitions to qualitatively explain how the photon hole-current drag effect arises. It may be assumed that, owing to the Kramers–Kronig relation, the hole-controlled refractive index of a hole semiconductor in the infrared region of the spectrum is due to virtual intersubband hole transitions (Fig. 1). The overall effect is obtained by summing up all possi-
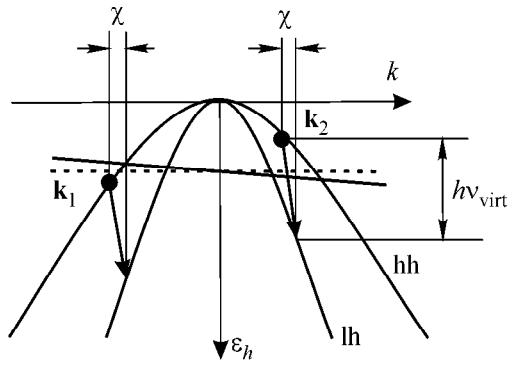
Fig. 1. Schematic representation of the light hole-current drag effect in diamond-like semiconductors. The dotted line indicates subband filling in the absence of current, and the dashed line illustrates the asymmetric distribution function in the presence of current.
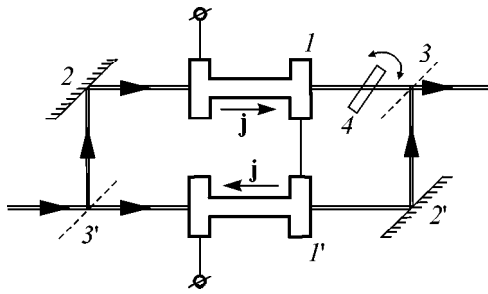
Fig. 2. Method of measuring the linear contribution of an electric field to the refractive index. (*1*, *1'*) Two identical Ge samples; (*2*, *2'*) nontransmitting mirrors; (*3*, *3'*) semitransparent mirrors; and (*4*) phase-shifting plate made from BaF_2.
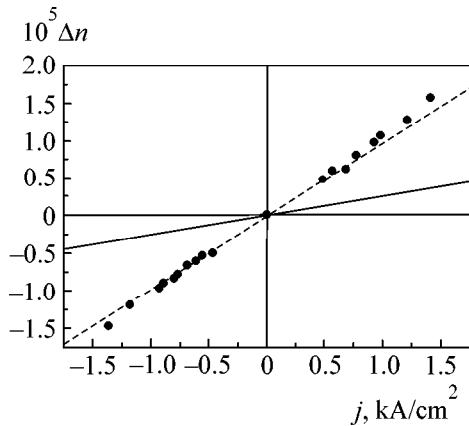
Fig. 3. Plot of the linear contribution to the refractive index of *p*-Ge vs. current density. The points are for the experiment, and the dashed straight line is the linear extrapolation from the weak-field region. The solid line corresponds to the lower estimate made by Eq. (3) for the magnitude of the effect. Temperature $T = 80$ K; the hole concentration is $N_h = 1.2 \times 10^{15}$ cm^{-3}; the sample length along the light direction is $L = 13$ mm; and $\mathbf{E} \| \mathbf{v}_{\partial p} \| [111]$.

ble transitions with regard to the hole momentum distribution.

With allowance made for the light wave vector, the intersubband transitions are nonvertical and occur, for the same photon energy, from the different initial energy states of holes with opposite wave-vector directions: $k_1 \neq k_2$ (Fig. 1). In the absence of a current, the total transition probabilities are identical for both directions, because the distribution function is symmetric. In the presence of hole drift, the hole distribution in **k** space becomes asymmetric and the transition probabilities for the photons with wave vectors χ and $-\chi$ become different, so that, owing to the Kramers–Kronig relation, the term depending linearly on the hole-current vector **j** and the light wave vector χ appears in the expression for the refractive index n: $\Delta n \propto (\mathbf{j} \cdot \chi)$.

Experimental results and discussion. A hole-type germanium was chosen as a model *p*-type semiconductor suitable for investigation. In strong electric fields, germanium exhibits a quadratic electrooptical Kerr effect [8]. To eliminate the influence of the quadratic electric-field corrections to the refractive index and other side effects on the experimental results, the configuration of the experiment was that shown in Fig. 2.

Two identical *p*-Ge samples were placed in each arm of a two-beam Mach–Zehnder interferometer. The samples were connected in such a way that the current and light directions were parallel in one of them and antiparallel in the other. The current pulse duration was equal to 0.2 ms. Therefore, the change Δn in the refractive index induces a phase shift between the waves passed through the different interferometer arms:

$$\delta = \frac{4\pi L}{\lambda}\Delta n. \qquad (4)$$

A CO_2 laser was used as a radiation source ($\lambda = 10.6$ μm). The intensity of polarized radiation passed through the interferometer was proportional to $\cos^2(\delta/2)$. To improve the sensitivity of the method, the operating point (initial phase shift) was chosen at the steepest portion of the characteristic by turning a transparent phase plate placed in one of the interferometer arms. An attendant and effect-masking radiation-intensity modulation caused by an electric-field-induced change in the intersubband absorption was allowed for by the supplementary measurements of transmittances in each of the interferometer channels.

A linear part of the experimentally measured change in refractive index is displayed in Fig. 3 as a function of the current density. The results of a simplified calculation by Eq. (3) yielding a lower estimate for the magnitude of the effect are presented for comparison in the same figure.

Only qualitative agreement between the calculation and experiment is observed. In our opinion, such is the case because the theory [6] used a number of simplified assumptions. Among these was the high-frequency approximation, according to which the energy of hot

holes was ignored, as compared to the photon energy $h\nu$, and the denominators of the $\mathcal{E}_1 - \mathcal{E}_2 \pm h\nu$ type ($\mathcal{E}_1$ and $\mathcal{E}_2$ are the energies of heavy and light holes, respectively) were replaced by the photon energy $h\nu$. This assumption works poorly in weak fields and not at all in strong fields. This is likely the reason why the magnitude of the effect increases with field superlinearly in the current. The superlinearity should also arise because of the nonparabolicity of the light-hole subband, which was ignored in the calculation [6].

Although photon hole-current drag was investigated in this work for hole-type germanium, it is clear that the mechanism described above is common to the majority of p-type semiconductors.

REFERENCES

1. L. D. Landau and E. M. Lifshitz, *Statistical Physics* (Nauka, Moscow, 1976; Pergamon, Oxford, 1980), Part 1.

2. T. S. Moss, G. J. Burrel, and E. Hetherington, Proc. R. Soc. London, Ser. A **308**, 125 (1968).

3. L. A. Almazov, F. T. Vas'ko, and I. M. Dykman, Pis'ma Zh. Éksp. Teor. Fiz. **16**, 305 (1972) [JETP Lett. **16**, 215 (1972)].

4. F. T. Vas'ko, Fiz. Tverd. Tela (Leningrad) **14**, 3680 (1972) [Sov. Phys. Solid State **14**, 3081 (1972)].

5. L. A. Almazov, Fiz. Tekh. Poluprovodn. (Leningrad) **9**, 657 (1975) [Sov. Phys. Solid State **9**, 433 (1975)].

6. F. T. Vas'ko and G. I. Steblovskiĭ, Ukr. Fiz. Zh. (Russ. Ed.) **32**, 673 (1987).

7. A. M. Danishevskiĭ, A. A. Kastal'skiĭ, S. M. Ryvkin, and I. D. Yaroshetskiĭ, Zh. Éksp. Teor. Fiz. **58**, 544 (1970) [Sov. Phys. JETP **31**, 292 (1970)].

8. L. E. Vorob'ev, D. V. Donetskiĭ, and D. A. Firsov, Pis'ma Zh. Éksp. Teor. Fiz. **59**, 832 (1994) [JETP Lett. **59**, 869 (1994)].

Translated by V. Sakun

========= **CONDENSED MATTER** =========

Resistance Quantum Oscillations in the Intermediate State of Singly Connected Pb and Sn Samples

Yu. N. Tsyan

Verkin Physicotechnical Institute of Low Temperatures, National Academy of Sciences of Ukraine, Kharkov, 61164 Ukraine
e-mail: chiang@ilt.kharkov.ua
Received March 16, 2000; in final form, March 22, 2000

The conductivities of hybrid NS structures of the intermediate state of type I Pb and Sn superconductors with large electron elastic mean free path were studied at helium temperatures. With changing temperature and critical magnetic field, the resistances of singly connected samples of these metals in the indicated state oscillate with a period corresponding to a change of a single quantum $hc/2e$ in the magnetic flux inside the normal region of an area on the order of 1 μm^2. The proposed quantum-interference scattering mechanism explains the nature and characteristic features of these oscillations. © *2000 MAIK "Nauka/Interperiodica"*.

PACS numbers: 72.15.-v; 74.80.Fp

Most of the experimental evidence for the occurrence of a quantum-interference contribution of coherent electrons to the kinetic properties of normal metals has been obtained for systems with weak electron localization, when coherent transport is only a small correction to diffusional transport (in mesoscopic samples with small electron elastic mean free path). Under these conditions, the oscillatory phenomena in a magnetic field can only be observed for samples with doubly connected geometry which allows the separation of coherent transport [1, 2]. In a hybrid "normal metal–type I superconductor" system (NS system), the contribution of the coherent excitations to the normal conductivity dominates on the distance scale on the order of a ballistic path from the NS boundary, irrespective of the system size, its connectivity, and, generally, the electron mean free path; due to Andreev reflection, the spectrum of coherent excitations is always resolved on this scale. If the scattering from elastic centers dominates and the metal is sufficiently pure, the scale becomes macroscopic. Studies of such systems have revealed an unusual behavior of the normal conductivity [3, 4], in line with the fundamental predictions about the specific features of coherent-excitation scattering in the vicinity of the NS boundaries [5–7]. This work presents new experimental data on these features. Studies of intermediate-state NS structures of singly connected type I superconductors with large electron elastic mean free path l_{el} revealed resistance quantum oscillations of a type similar to the Aharonov–Bohm effect.

The temperature-dependent resistances of Pb plates and Sn constriction were studied. The intermediate state was maintained by applying a weak external transverse magnetic field $\mathbf{B}_e$ to the plates and by a self-current field $\mathbf{B}_I$ in the constriction. The Pb plate sizes were $x \times y \times z = L \times w \times t = 3$ mm $\times$ (0.23–1.5) mm $\times$

(≈ 20 μm), with a separation of $L_m \approx 250$ μm between the measuring probes in the middle part of the samples. $\mathbf{B}_e = [0,0,480$ G], [0,0,550 G], and [0,0,–520 G]. The tin constriction was $t \approx 20$ μm in diameter and $L \approx 50$ μm in length, with $L_m \approx 100$ μm. At the constriction surface, $\mathbf{B}_I \approx 100$ G at $I \approx 1$ A. The samples are schematically represented in Figs. 1 and 2. The bulk elastic mean free path in the workpieces from which the samples were fabricated was $l_{el} \sim 100$ μm. It virtually did not change in the Pb plates and decreased by approximately an order of magnitude in the Sn constriction (the estimates were made with allowance for the size and magnetoresistive effects).

The deviation ΔU of the potential difference from its mean (monotonic) value $\overline{U}$ was taken into account only in the temperature range where $(\Delta U)_{max}/\overline{U}$ exceeded the total measurement error $\delta_m = \delta U/U + \delta_\Sigma$ by no less than an order of magnitude. $\delta U/U$ and δ_Σ are the relative measurement errors, respectively, for the bias voltage and all other attendant parameters: temperature, currents, and external magnetic field. This condition was confidently satisfied below ca. 3 K for the plates and 3.5 K for the constriction at a $\overline{U}$ resolution of up to the $\delta U = (10^{-11}–10^{-12})$ V level [8]. For instance, in the Pb plate for which the results are presented, $(\Delta U)_{max}/\overline{U} = 2\%$, $\delta_m \approx 0.2\%$ ($\approx \delta U/U > \delta_\Sigma \approx 0.03\%$), $\overline{U} = 5.87 \times 10^{-8}$ V at 3 K and $(\Delta U)_{max}/\overline{U} = 200\%$, $\delta_m \approx 10\%$ ($\approx \delta U/U \gg \delta_\Sigma$), and $\overline{U} = 3.24 \times 10^{-10}$ V at 2 K; $I = 1$ A. For the Sn constriction, $(\Delta U)_{max}/\overline{U} = 0.1\%$, $\delta_m \approx 0.03\%$ ($\approx \delta U/U = \delta_\Sigma \approx 0.01\%$), $\overline{U} = 4.3402 \times 10^{-6}$ V at 3.5 K and $\Delta U/\overline{U} = 1\%$, $\delta_m \approx 0.1\%$ ($\approx \delta_\Sigma \gg \delta U/U \approx$

0.01%), and $\overline{U} = 4.0029 \times 10^{-6}$ V at 2 K; $I = 1$ A. One can see that $(\Delta U)_{max}/\overline{U} \geq 10\delta_m$ in the respective temperature ranges.

The typical features of the resistance R of the Pb plates are demonstrated in Fig. 1, where the temperature derivative of R is shown for one of the plates ($w = 0.23$ mm). The temperature dependence of the resistance of the Sn constriction is shown in Fig. 2. It follows from these graphs that the resistances of the samples oscillate with temperature in the fields maintaining the intermediate state. The oscillating resistance components $\Delta R \equiv \Delta U/I = R - \overline{R}$ (hereafter, R-oscillations) are shown separately in the insets in Fig. 2 for the Sn constriction and in Fig. 3 for the Pb plate. As is seen, the oscillation amplitude $(\Delta R)_{max}$ weakly depends on the temperature and the external magnetic field (although the monotonic resistance components vary over no less than two orders of magnitude). The character of oscillations in the Pb plate at various B_e values (Fig. 3) is evidence that the oscillation phase ϕ depends on the strength and sense of the external magnetic field: $\phi_{480\,G}$ is shifted from $\phi_{550\,G}$ by approximately π, while $\phi_{520\,G}$ and $\phi_{550\,G}$ coincide.

Constructing the critical-field scale for the oscillation region according to the $B_c(T) \simeq B_c(0)\{1 - [T/T_c(0)]^2\}$ equation (T_c is the superconducting transition critical temperature, $B_c^{Pb}(0) = 803$ G, and $B_c^{Sn}(0) = 305$ G [9]), one finds that Δ_B is constant for any pair of points one period apart and is equal to the difference in the absolute values of the critical field (see Fig. 3 and the inset in Fig. 2) for each of the samples. This suggests that the $\Delta_B(B_c)$ period is a function of the direct, rather than the reversed, field. The temperature T_0 corresponding to the onset of R-oscillations in the Sn constriction is equal to the temperature for which $B_c^{Sn}(T_0) = B_I$ (≈ 100 G), i.e., the temperature of the appearance of the intermediate state (recall that the conditions for the confident resolution of the oscillations were fully satisfied for this sample up to 3.5 K). With $\mathbf{B}_e$ used for the Pb plate, T_0 should lie outside the range of helium temperatures.

The dependence of the magnitude of the effect on the critical field in the intermediate state, first, provides direct evidence for the presence of a laminar domain NS structure and, second, indicates that the mechanism responsible for the R-oscillations occurs in the normal areas of domains, where, as is known, the magnetic field is equal to the superconductor critical field $\mathbf{B}_c(T)$ [10]. The use of the phenomenological theory of superconductivity [10, 11] for estimating the number of domains between the measuring probes brought about the values of approximately 12 at 3 K and 16 at 1.5 K for the Pb plate, 1 or 2 for the Sn constriction, and the value of 15–22 μm for the distance d_n between the NS boundaries in the oscillation region of interest. These data suggest the lack of any correlation between the
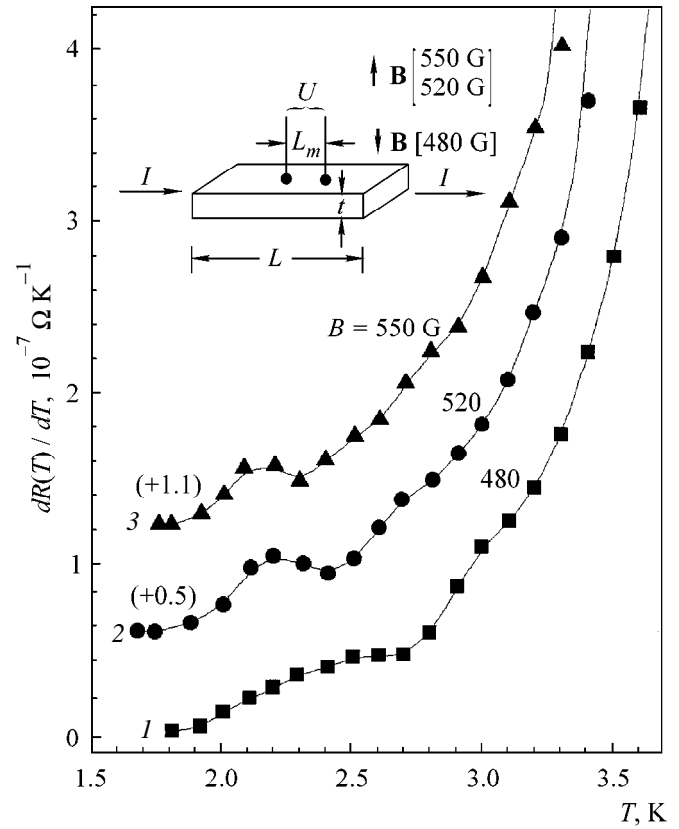
Fig. 1. Temperature derivative of the effective resistance $R = U/I$ of the intermediate-state Pb plate in external magnetic fields of different strengths (curves *2* and *3* are shifted relative to curve *1*).
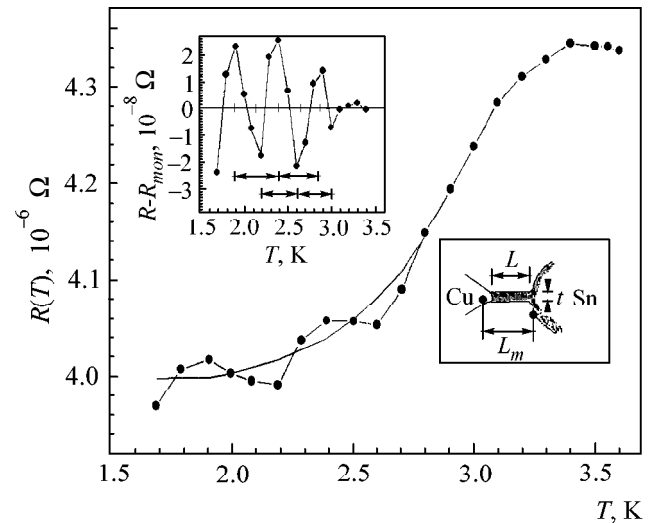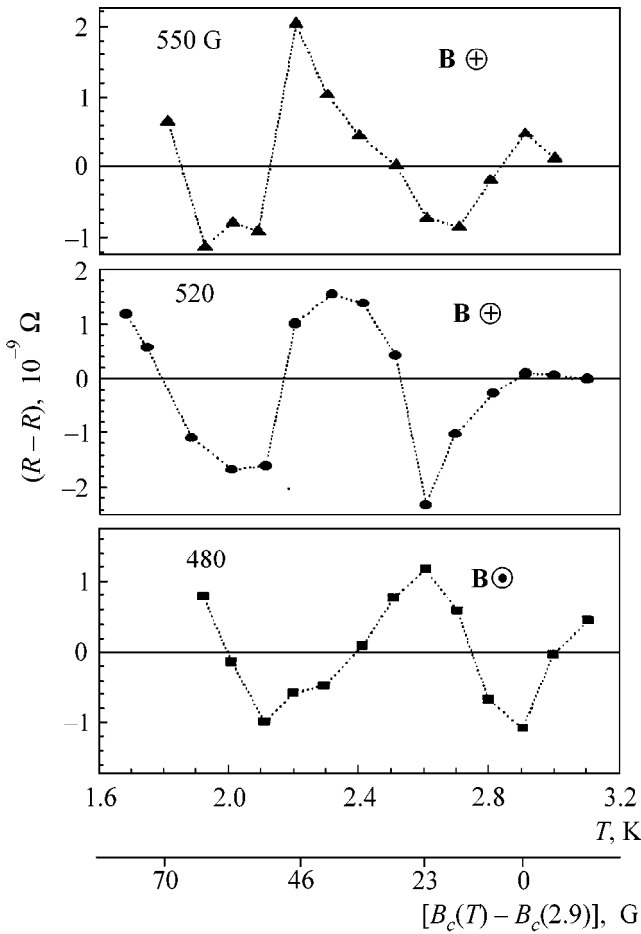

Fig. 2. Temperature dependence of the effective resistance of the intermediate-state Sn constriction in a self-current magnetic field. Inset: *hc/2e* oscillations of the effective resistance; arrows indicate 50-G intervals.

Fig. 3. The *hc/2e* oscillations of the effective resistance of a Pb plate in the intermediate state.

indicated numbers and the number of observed oscillation periods.

As is known, the direct dependence of the oscillation phase on the field strength arises when the quantization is associated with a real-space "geometric" factor, i.e., with the interference of coherent excitations on the geometrically specified closed dissipative trajectories in a magnetic vector-potential field [12, 13]. At distances on the order of the thermal length $\lambda_T \approx \hbar v_F/k_B T$ from the NS boundary, where $l_{el} \gg \lambda_T$, those coherent trajectories on which the elastic-scattering center (impurity) interacts simultaneously with the coherent *e* (usual) and *h* (Andreev) excitations, are the main type of dissipative trajectories [5, 6]. It was demonstrated in [5] that, owing to the doubled probability of the *h* excitations being scattered by the impurity, the interference on these trajectories generates the *R*-oscillations. In the presence of an electric field alone, neither the impurity nor the relevant coherent-trajectory size are set off, so that the oscillations do not arise [6, 7].

Since the *e* and *h* trajectories spatially diverge in a magnetic field, the distance *r* from the impurity to the outermost boundary point, from which the particle can

return to the same impurity after the Andreev reflection, is bounded, according to the simple classical geometric considerations, by the value

$$r \approx 2(qR_L)^{1/2}. \quad (1)$$

In Eq. (1), R_L is the Larmor radius and *q* is the parameter (on the order of a shielding radius) characterizing the impurity size. For instance, in fields of several hundred Gauss, $R_L \approx 1.5 \times 10^{-2}$ cm and *r* does not exceed (1–2) μm at $q \approx (2-5) \times 10^{-8}$ cm; i.e., $\xi_0 < r \le \lambda_T \sim 10^{-2}l_{el}$ ($l_{el} \gg d_n$, λ_T; $\lambda_T \approx 3$ μm). Therefore, for every impurity with coordinate *z*, the magnetic field specifies in the $z = $ const plane a finite region of possible coherent trajectories passing through the impurity and closing two arbitrary reflection points on the NS boundary between the two most distant points whose positions are determined by Eq. (1). After averaging over all impurities, only a single trajectory (or a group of identical trajectories) specified by the edge of integration over the quantization area *A* makes an uncompensated contribution to the wave-function phase. The integration edge $A_{edge} = \frac{1}{2} r_{q_{max}}^2$ corresponds to the area bounded by the trajectory passing through the most efficient (with q_{max}^2) impurity situated at a maximum distance from the boundary, as allowed by criterion (1). One can easily verify that, in our samples with $l_{el} \le 0.1$ mm, every layer of impurity-size thickness parallel to the NS boundary comprises no less than 10^3 impurities; i.e., the coherent trajectories corresponding to the integration edge continuously resume upon shifting or the formation of new NS boundaries, so that A_{edge} is a continuously defined constant accurate to $q_{max}/r_{q_{max}} \sim 10^{-4}$.

According to [2, 4], the wave-function phase for the excitations with energy $E = eU$ in the field *B* should change on a coherent trajectory of length Λ as

$$\phi = \phi_e + \phi_h = 2\pi \left[(1/\pi)(E/\hbar v_F)\Lambda + \frac{BA}{\Phi_0/2} \right], \quad (2)$$

where $\Phi_0 = hc/e = 4.14 \times 10^{-7}$ G cm². The first term in Eq. (2) can be ignored because, in our samples, it does not exceed 10^{-5} at $U \le 10^{-8}$ V. One can thus expect that the interference contribution coming from the elastic-scattering centers to the conductivity and caused by the difference in the scattering probabilities for *e* and *h* [2] will oscillate in the range $B \equiv B_c(T) - B_c(T_0)$ as $\Delta R_{osc} \cos\phi$, where

$$\phi = 2\pi \frac{[B_c(T) - B_c(T_0)]A_{edge}}{\Phi_0/2}, \quad (3)$$

with the amplitude ΔR_{osc} depending on the concentration of the most efficient scattering centers and, hence, proportional to the total concentration *c*.

From the $\Delta_B A_{edge} = \Phi_0/2$ condition and $\Delta_B \approx (45; 50)$ G, one obtains $r \approx 1$ μm, in accordance with the above independent estimate. The ratio of the oscillation amplitudes also conforms to its expected value: $[(\Delta R_{osc})^{Sn}/(\Delta R_{osc})^{Pb}] \sim (c^{Sn}/c^{Pb}) \sim (l_{el}^{Pb}/l_{el}^{Sn}) \sim 10$. One can expect that a change in the number of domains in the plate from 12 to 16 will alter the oscillation amplitude by no more than 40%; i.e., it will only modify the oscillations but not break the overall periodicity pattern (Fig. 3). It also follows from Eq. (3) that the number of periods between the point T_0 of oscillation onset and the arbitrary temperature depends on the $B_c(T_0) = B_e$ value. This makes understandable the ratio of phase oscillations observed for the Pb plate in different fields: $\phi_{550\,G} - \phi_{480\,G} \approx 3\pi$ and $\phi_{520\,G} - \phi_{480\,G} + \pi \approx 3\pi$ (it is taken into account that $\mathbf{B}[520\,G] = -\mathbf{B}[480\,G]$).

In conclusion, let us formulate the main results of the work. The conductivities of hybrid NS structures of the intermediate state of type I Pb and Sn superconductors with large electron elastic mean free paths were experimentally measured. In this state, the resistances of singly connected samples of the cited metals oscillate with changing temperature and critical magnetic field. The phase and period of R-oscillations are functions of the direct values of this field. The oscillation period corresponds to a change of a single flux quantum $hc/2e$ in the magnetic flux inside the region of area on the order of 1 μm^2. The oscillation phase is sensitive to the sense and strength of an external magnetic field. The oscillation amplitude weakly depends on temperature, as opposed to the monotonic component, which varies over several orders of magnitude. The proposed quantum-interference mechanism of scattering by elastic centers explains the nature and the above-mentioned features observed for the resistance oscillations. The mechanism is based on the criterion for spatial constraints on the interaction of coherent excitations with the elastic-scattering centers in magnetic field.

REFERENCES

1. S. Washburn and R. A. Webb, Adv. Phys. **35**, 375 (1986).
2. A. G. Aronov and Yu. V. Sharvin, Rev. Mod. Phys. **59**, 755 (1987).
3. Yu. N. Chiang and O. G. Shevchenko, Zh. Éksp. Teor. Fiz. **113**, 1064 (1998) [JETP **86**, 582 (1998)].
4. Yu. N. Chiang and O. G. Shevchenko, Fiz. Nizk. Temp. **25**, 432 (1999) [Low Temp. Phys. **25**, 314 (1999)].
5. J. Herath and D. Rainer, Physica C (Amsterdam) **161**, 209 (1989).
6. B. J. van Wees, P. de Vries, P. Magnic, and T. M. Klapwijk, Phys. Rev. Lett. **69**, 510 (1992).
7. A. Kadigrobov, R. Shekhter, and M. Jonson, Physica B (Amsterdam) **218**, 134 (1996).
8. Yu. N. Chiang, Prib. Tekh. Éksp. **1**, 202 (1981).
9. *Handbook of Chemistry and Physics* (Cleveland, Chem. Rub., 1974–1975).
10. P. G. De Gennes, *Superconductivity of Metals and Alloys* (Benjamin, New York, 1966).
11. E. M. Lifshitz and Yu. V. Sharvin, Dokl. Akad. Nauk Ukr. SSR **79**, 783 (1951).
12. Y. Aharonov and D. Bohm, Phys. Rev. **115**, 485 (1959).
13. B. L. Altshuler, A. G. Aronov, and B. Z. Spivak, Pis'ma Zh. Éksp. Teor. Fiz. **33**, 101 (1981) [JETP Lett. **33**, 94 (1981)].

Translated by V. Sakun

═══ CONDENSED MATTER ═══

Overlap Integral for Quantum Skyrmions[1]

R. A. Istomin and A. S. Moskvin

Department of Theoretical Physics, Ural State University, pr. Lenina 51, Yekaterinburg, 620083 Russia

e-mail: Roman.Istomin@usu.ru

Received December 28, 1999; in final form, March 28, 2000

Making use of the method of spin coherent states, we obtained an analytical form of the overlap integral for quantum skyrmions. © *2000 MAIK "Nauka/Interperiodica".*

PACS numbers: 75.10.Jm; 03.65.Sq

Skyrmions are general static solutions of 2D Heisenberg ferromagnets obtained by Belavin and Polyakov [1] from the classical nonlinear sigma model. A renewed interest in these unconventional spin textures is stimulated by the high-T_c problem in doped quasi-2D cuprates and the quantum Hall effect.

The spin distribution within classical skyrmions of topological charge $q = 1$ is given as follows:

$$S_x = \frac{2r\lambda}{r^2 + \lambda^2}\cos\varphi, \quad S_y = \frac{2r\lambda}{r^2 + \lambda^2}\sin\varphi,$$

$$S_z = \frac{r^2 - \lambda^2}{r^2 + \lambda^2}. \tag{1}$$

In terms of the stereographic variables, a skyrmion with radius λ and phase φ_0 centered at a point z_0 is identified with spin distribution $w(z) = \Lambda(z - z_0)$, where $z = x + iy = re^{i\varphi}$ is a point in the complex plane $\Lambda = \lambda e^{i\theta}$ and is characterized by three modes: translational z_0-mode, "rotational" θ-mode, and "dilatational" λ-mode. Each of them relates to a certain symmetry of the classical skyrmion configuration. For instance, θ-mode corresponds to a combination of rotational symmetry and internal $U(1)$ transformation.

The simplest wave function of the spin system, which corresponds to a classical skyrmion, is a product of spin coherent states [2]. In the case of spin $s = 1/2$,

$$\Psi_{sk}(0)$$

$$= \prod_i \left[\cos\frac{\theta_i}{2}\exp\left\{i\frac{\varphi_i}{2}\right\}|\uparrow\rangle + \sin\frac{\theta_i}{2}\exp\left\{-i\frac{\varphi_i}{2}\right\}|\downarrow\rangle \right], \tag{2}$$

where $\theta_i = \arccos(r_i^2 - \lambda^2)/(r_i^2 + \lambda^2)$. Coherent state implies a maximum equivalence to the classical state with minimal uncertainty of spin components. In this connection, we should note that such a state was used

in [3] by Schliemann and Mertens, where an expression for the square variance of the Heisenberg Hamiltonian was obtained.

Classical skyrmions with different phases and radii have equal energy. Nevertheless, the stationary state of a quantum skyrmion of topological charge $q = 1$ is not a superposition of states with different phases and radii [4] but has a certain distinct value of λ.

In this paper [5], we consider some features of the quasiparticle behavior for the quantum skyrmion. First of all, it implies the calculation of the overlap and "resonance" integrals $S_{12} = \langle\Psi_{sk}(\mathbf{R}_1)|\Psi_{sk}(\mathbf{R}_2)\rangle$, $H_{12} = \langle\Psi_{sk}(\mathbf{R}_1)|\hat{H}|\Psi_{sk}(\mathbf{R}_2)\rangle$.

As a helpful illustration to the calculation of the overlap integral for quantum topological defects, it is worth presenting some known results concerning the overlap of vortices in a 2D superconducting condensate [6]. Phenomenologically, such vortices were described as pointlike quasiparticles moving under the action of the transverse Magnus force. The coherent state of a vortex with a center in $\mathbf{R}_0$ was taken in the form [6]

$$|\Psi_{sk}(\mathbf{R}_0)\rangle = \frac{1}{\sqrt{2\pi l^2}}\exp\left[-\frac{|\mathbf{r} - \mathbf{R}_0|^2}{4l^2} + \frac{i\mathbf{z}\cdot\mathbf{R}_0\times\mathbf{r}}{2l^2} \right], \tag{3}$$

where ρ_0 is the density of the 2D condensate, $l = (2\pi\rho_0)^{-1/2}$ is the average distance between particles in the condensate, and $\mathbf{z}$ is unit vector normal to the plane of the condensate. The overlap integral for two coherent states is then easily calculated as

$$S_{12} = \langle\Psi_{sk}(\mathbf{R}_1)|\Psi_{sk}(\mathbf{R}_2)\rangle$$

$$= \exp\left[-\frac{1}{4l^2}(R_{12}^2 - 4i\Delta_{12}) \right], \tag{4}$$

where

$$\Delta_{12} = \frac{1}{2}\mathbf{z}\cdot[\mathbf{R}_1\times\mathbf{R}_2], \quad R_{12} = |\mathbf{R}_1 - \mathbf{R}_2|.$$

---

[1] This article was submitted by the authors in English.

It contains a Gaussian factor reflecting the localization of the coherent state and also a specific phase factor Δ_{12}, being the area of a sector the topological defect covers while moving in the plane. This factor originates from the phase factor in function (3), typical for a charged particle moving in a magnetic field or, in general, for a particle which experiences the Magnus force. The correct form of such a Magnus force for an out-of-plane magnetic vortex with the topological charge $\frac{1}{2}$ ("half-skyrmion") was derived by Nikiforov and Sonin [7], the Magnus force acting on the classical skyrmion being simply twice as large [8].

As is seen, Eq. (4) reflects two common features of the overlap integral for the topological defects in a 2D system, namely, the Gaussian dependence on R_{12} and the presence of the Berry phase. One should note that in a recent paper by Thang [9], it is shown that wave function (3) does not provide a correct description of the transition to the infinite system, when the overlap integral turns to zero. Nevertheless, Eqs. (3) and (4) for the wave function and overlap integral allow one to elucidate many generic features of the corresponding quantities for the topological defects.

To reveal some features of the quantum quasiparticle behavior for skyrmions, we consider the overlap integral for a simple quantum state, like (2), of spin system with skyrmion $\lambda/(z - R_1)$ at the point $R_1 = |R_1|e^{i\varphi_1}$ with the state $\lambda/(z - R_2)$, which corresponds to the skyrmion shifted to an arbitrary distance

$$R_1^2 = |R_1|^2 + |R_2|^2 - 2R_1 R_2 \cos(\varphi_1 - \varphi_2)$$

into the point $R_2 = |R_2|e^{i\varphi_2}$. The overlap of the single spin coherent states characterized by two different points in the complex plane ς and μ is [2]

$$\langle \varsigma | \mu \rangle = \frac{(1 + \varsigma\bar{\mu})^{2S}}{(1 + |\varsigma|^2)^S (1 + |\mu|^2)^S}. \tag{5}$$

Thus, the overlap integral for the skyrmion states is given by

$$S_{12}^{\lambda\lambda} = \prod_i \frac{(1 + \varsigma\bar{\mu})^{2S}}{(1 + |\varsigma|^2)^S (1 + |\mu|^2)^S}$$

$$= \exp\left(S \sum_i \ln\left[\frac{(1 + \varsigma\bar{\mu})^2}{(1 + |\varsigma|^2)(1 + |\mu|^2)} \right] \right)$$

$$= \exp\left(S \sum_i \left[2\ln\left(1 + \frac{\lambda^2}{r_i^2 + R_1\overline{R}_2 - r_i R_1 e^{-i\varphi_i} - r_i \overline{R}_2 e^{+i\varphi_i}} \right) \right. \right.$$

$$\left. \left. - \ln\left(1 + \frac{\lambda^2}{r_i^2 + R_2^2 - 2R_2 r_i \cos\varphi_i} \right) \right. \right. \tag{6}$$

$$\left. \left. - \ln\left(1 + \frac{\lambda^2}{r_i^2 + R_1^2 - 2R_1 r_i \cos\varphi_i} \right) \right] \right)$$

$$= \exp(2I(R_1, R_2) - I(R_1, R_1) - I(R_2, R_2)).$$

It should be noted that for displacements $R \geq 2\lambda$ in the continuous complex plane the overlap integral turns to zero, since in this case there exist two such points for which the initial and the final spin states are orthogonal. For example, in the case of $R_1 = 0$, $R_2 = R$, where R is real, $1 + \lambda^2/z(z - R) = 0$ when $z = R/2 \pm \sqrt{R^2/4 - \lambda^2}$. However, the overlap of the skyrmion on the lattice turns to zero only at certain values of R, which form a certain discrete set of values. In particular, for the displacement along the direction of the elementary vector of the lattice, the overlap is identically zero at the points $R = (\lambda^2 + k^2)/k$ given integer k.

To consider the skyrmions of large radius, we turn the sum in the exponent of Eq. (6) into an integral. The quantity c/λ for large skyrmions is small and we virtually need to keep the terms of zero order in c/λ, with c being the lattice constant. Spin density, that is, the number of spins in the unit cell of the plane, is simply $1/c^2$. Theory will be invariant with respect to the scale transformations, that is, to the variations of c and simultaneous equivalent variations of λ and R. In addition, we consider the size L of the system to be much larger than the skyrmion size and virtually keep only the terms of zero order in λ/L. To this end, we may merely set $L = \infty$. Thus, the result is

$$I(R_1, R_2) = \frac{1}{c^2} \int_0^\infty A(r, R_1, R_2) r \, dr, \tag{7}$$

where

$$A(r, R_1, R_2)$$
$$= \int_0^{2\pi} d\varphi \ln(\lambda^2 + r^2 + R_1\overline{R}_2 - rR_1 e^{-i\varphi} - r\overline{R}_2 e^{+i\varphi}). \tag{8}$$

In order to perform the angular integration in $A(r, R_1, R_2)$, we introduce the complex variable $z = e^{+i\varphi}$, so that

$$A(r, R_1, R_2)$$
$$= \int dz \frac{\ln(\lambda^2 + r^2 + R_1\overline{R}_2 - rR_1 z^{-1} - r\overline{R}_2 z)}{iz}, \tag{9}$$

where the integration is taken on a circle of unit radius. This integral turns out to be nonzero due to the pole in $z = 0$ and the nonanaliticity area associated with the existence of a cut in the space of values of the complex logarithm when its argument is negative. While crossing the axis of negative values of the argument the phase jumps from $-\pi$ to π. In the plane of z nonanaliticity, the area is the curve given by the equation

$$\mathrm{Im}(\lambda^2 + r^2 + R_1\overline{R}_2 - rR_1 z^{-1} - r\overline{R}_2 z) = 0,$$

$$\mathrm{Re}(\lambda^2 + r^2 + R_1\overline{R}_2 - rR_1 z^{-1} - r\overline{R}_2 z) < 0.$$

For $R > 2$, there exists an interval of r values for which the end of the cut lies on the border of the unit circle, resulting in a purely imaginary contribution to the integral $A(r, R_1, R_2)$. The range of r in which this occurs is given by the interval $[r_1, r_2]$, where

$$r_{1,2}^2 = (|R_1|^2 + |R_1|^2)/2 - \lambda^2 \pm (|R_1|^2 - |R_1|^2)\sqrt{\frac{1}{4} - \frac{\lambda^2}{R^2}}.$$

As a result of the existence of the cut, we have the following expression for the integral:

$$A(r, R_1, R_2) = 2\pi\begin{cases} \ln\left(\dfrac{\lambda^2 + r^2 + R_1\overline{R}_2 + \sqrt{(\lambda^2 + r^2 + R_1\overline{R}_2)^2 - 4r^2 R_1\overline{R}_2}}{2}\right), & \text{if } r > r_2 \text{ or } r < r_1 \\[2ex] \ln(rR_1) - i\arcsin y(r), & \text{if } r_1 < r < r_2, \end{cases}$$

where

$$y(r) = |R_2|\sin f$$

$$\times \frac{-|R_1|^2 + |R_1||R_2|\cos f + \sqrt{r^2 R^2 - |R_1|^2|R_2|^2 \sin^2 f}}{rR^2},$$

with f being the phase difference between R_1 and $\overline{R}_2$. Similar expressions exist for $A(r, R_1, R_1)$ and $A(r, R_2, R_2)$. With allowance made for the obvious identity

$$((\lambda^2 + r_1^2 + R_1\overline{R}_2)^2 - 4r_1^2 R_1\overline{R}_2)$$

$$- ((\lambda^2 + r_2^2 + R_1\overline{R}_2)^2 - 4r_2^2 R_1\overline{R}_2)$$

$$= (R^2 + 2i\sin f|R_1||R_2|)\sqrt{\frac{1}{4} - \frac{\lambda^2}{R^2}}(|R_1|^2 - |R_2|^2)$$

and integration in Eq. (7), we finally obtain for the overlap integral

$$S_{12} = \exp\left[-\frac{\pi S}{c^2}(R_{12}^2 - 4i\Delta_{12})\right], \qquad (10)$$

if $R_{12} < 2\lambda$ or

$$S_{12} = \exp\left[-\frac{S\pi}{c^2}\left(R_{12}^2 - 4i\Delta_{12} - R_{12}\sqrt{R_{12}^2 - 4\lambda^2}\right.\right.$$

$$\left.\left. + 2\lambda^2\ln\left(\frac{R_{12} + \sqrt{R_{12}^2 - 4\lambda^2}}{R_{12} - \sqrt{R_{12}^2 - 4\lambda^2}}\right)\right)\right], \qquad (11)$$

if $R_{12} > 2\lambda$. As above in Eq. (3), here Δ_{12} is the area of the sector the skyrmion covers while moving in the plane. Having wandered along a closed contour on the plane, the skyrmion acquires the phase $4\pi S(\Delta_{12}/c^2)$; that is, the skyrmion accumulates a phase of $4\pi S$ for every spin it encircles. Thus, its quantum motion looks like that of either a charged particle with unit charge in a uniform magnetic field of strength $4\pi\hbar S/c^2$ [10] or a particle

which experiences the transverse Magnus force $[\mathbf{b} \times \mathbf{v}]$, where $\mathbf{b} = 4\pi\hbar S\mathbf{z}/c^2$ and $\mathbf{v}$ is velocity, so that the corresponding length scale is $(4\pi S/c^2)^{-1/2}$, which is similar to the magnetic length. This is the same Magnus force that acts on the classical skyrmion [8] and that is simply twice as large as the one acting on the out-of-plane magnetic vortex with the topological charge $\frac{1}{2}$ ("half-skyrmion") [7].

One should note the specific dependence of the overlap integral on the spin-site density $(1/c^2)$ and the number of spin deviations $(2S)$, similar to the density dependence in Eq. (3).

When $R \longrightarrow \infty$, the R-dependence of the overlap integral obeys the power law

$$S_{12} = \left(\frac{\lambda^2}{R^2}\right)^{S2\pi\lambda^2/c^2} e^{-S2\pi\lambda^2/c^2}.$$

The expressions for the overlap of skyrmions were obtained in a continuous approximation, which is generally not correct in the vicinity of those values of displacements $R_{12} > 2\lambda$ at which the overlap of the distinct spin states is zero. Nonetheless, direct numerical calculation for sufficiently large 2D lattices shows that the logarithm of the skyrmion overlap integral is "almost everywhere" satisfactorily described by the continuous Eq. (11), except for a discrete set of R_{12} values in which the logarithm goes to $-\infty$.

We considered throughout the overlap of the skyrmions with equal λ, that is, with equal global phases and radii. It is easy to see that the skyrmion states with different λ and phases are orthogonal: $S_{12}^{\lambda\varphi\lambda'\varphi'} \propto \delta_{\lambda\lambda'}\cdot\delta_{\varphi\varphi'}$, which agrees with the "conservation law" for the quantity λ and phase in the skyrmion [4].

In conclusion, we used a simplified form for the quantum skyrmion wave function to obtain the analytical expression for the appropriate overlap integral whose form confirms the known statement [7, 8, 10] that the skyrmion moves like a particle in a uniform

magnetic field or a particle which experiences the Magnus force. We hope that making use of a more realistic wave function will keep the principal features of the result derived above.

We would like to thank G. Volovik and J. Schliemann for helpful comments and N. Mikushina for useful collaboration.

REFERENCES

1. A. A. Belavin and A. M. Polyakov, Pis'ma Zh. Éksp. Teor. Fiz. **22**, 245 (1975) [JETP Lett. **22**, 245 (1975)].

2. A. M. Perelomov, *Generalized Coherent States and Their Applications* (Nauka, Moscow, 1987; Springer-Verlag, Berlin, 1986).

3. J. Schliemann and F. G. Mertens, J. Phys.: Condens. Matter **10**, 1091 (1998).

4. A. Stern, Phys. Rev. Lett. **59**, 1506 (1987).

5. R. A. Istomin and A. S. Moskvin, cond-mat/9912048.

6. Q. Niu, P. Ao, and D. J. Thouless, Phys. Rev. Lett. **72**, 1706 (1994).

7. A. Nikiforov and E. Sonin, Zh. Éksp. Teor. Fiz. **85**, 642 (1983) [Sov. Phys. JETP **58**, 373 (1983)].

8. G. Volovik, Czech. J. Phys. Suppl. **46** (S2), 913 (1996); cond-mat/9603197.

9. J. M. Tang, cond-mat/9812438.

10. M. Stone, cond-mat/9512010.

CONDENSED MATTER

Band Structure Observed in the Current–Voltage Characteristics of SININIS-Type Junctions[1]

I. P. Nevirkovets*, ** and J. B. Ketterson*

* Northwestern University, Department of Physics and Astronomy, Evanston IL 60202, USA
e-mail: i-nevirkovets@nwu.edu
** Institute of Metal Physics, National Academy of Sciences of Ukraine, pr. Vernadskogo 36, Kiev, 252142 Ukraine
Received January 25, 2000; in final form, March 28, 2000

Band structure in the conductivity of 4-barrier Nb/Al–AlO$_x$–Al–AlO$_x$–Al–AlO$_x$–Al–AlO$_x$–Nb (SININIS) tunnel junctions is observed at low temperatures. This structure is explained in terms of the interference of quasiparticle waves in a periodic barrier. © 2000 MAIK "Nauka/Interperiodica".

PACS numbers: 74.50.+r; 74.80.Dm; 71.20.-b

Until recently, it was thought that the phase-coherent effects between the external S electrodes are negligibly small at nonzero voltage in SINIS-type junctions (here, N is either a normal metal or a superconductor with an energy gap Δ_N considerably smaller than that in S; I is an insulator) not having high-transparency barriers [1]. Later, it was shown experimentally and theoretically that such effects may be observed in the current–voltage characteristics (CVC) of SINIS junctions due to the interference of quasiparticle waves which are Andreev- and normally reflected at the tunnel barriers [2, 3]. However, the coherent effects observed so far in the CVC of double-barrier junctions consisting of a metallic thin-film N electrode manifest themselves either as a zero-voltage supercurrent enhancement [2] or as an increase in the conductivity at nonzero voltages [3]. At the same time, the minima in the conductivity were reported for mesoscopic S–Sm–S junctions in the subgap voltage region (here Sm denotes a doped semiconductor) [4] and, very recently, in the conductivity of HTSC-based junctions [5].

In this letter, we present experimental data showing that coherent coupling exists between S electrodes in multibarrier SININIS junctions involving low-T_c superconductors. As a result, a band structure in the conductivity appears, with minima nearly periodically positioned in voltage.

We have fabricated and investigated 4-barrier Nb/Al–AlO$_x$–Al–AlO$_x$–Al–AlO$_x$–Al–AlO$_x$–Nb junctions. We used the fabrication procedure that is now standard for Nb/Al–AlO$_x$–Al–AlO$_x$–Nb junctions, but included a slight deliberate contamination of part of the internal Al layers by oxygen [6]. The thickness of the external Nb electrodes was approximately 100 nm, whereas the thickness of the Al layers was 7 nm. The

junctions were patterned in a two-terminal configuration, so that the CVC could be measured only between the bottom and top S electrodes. The CVCs of a 10×10-μm device (sample 1) measured at $T = 4.2$ K and $T = 1.8$ K are shown in Fig. 1 (curves *a* and *b*, respectively). The overall shape of the curves is similar to that of a SIN-junction; i.e., the current rise begins at a voltage $V = \Delta_{Nb}/e$ and not at the voltage $V = 2\Delta_{Nb}/e$ (here, Δ_{Nb} is the superconducting energy gap of Nb), as might intuitively be expected. We also observed this behavior in SINIS junctions involving a thick middle N layer (with the thickness d_N exceeding the electron mean free path). The nature of this feature will be considered elsewhere. Here we only note that the shape of the CVC does not correspond to the simple series connection of the junctions that are involved in the system; i.e., the SININIS system behaves like a single junction of a new type.

The CVC measured at $T = 4.2$ K is smooth, while that measured at $T = 1.8$ K reveals steplike features accompanied by voltage "jumps." The features are nearly periodically spaced at a voltage of $V \simeq 1.2$ mV and persist up to $V \approx 6$ mV, which is higher than the gap sum voltage (even if a reasonable gap $\Delta_{Al} \approx 0.2$ meV is assigned to the Al N-layers [6]). The first feature appears near zero voltage as a high-conductivity resistive branch (see Fig. 1). This nearly periodical structure will be referred to as the band structure.
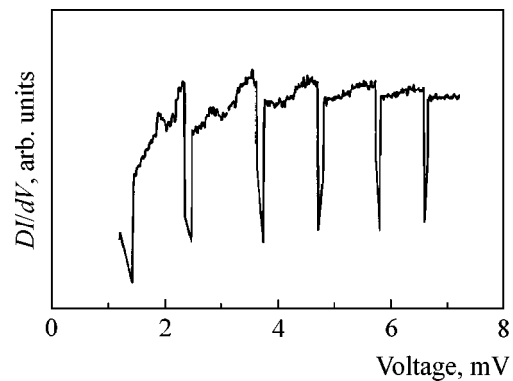
The band structure can be more clearly seen from the first derivative $dI/dV(V)$ of the CVC (see Fig. 2). The derivative was numerically calculated from a branch of the CVC recorded for increasing current (at $T = 1.8$ K) for a sample 2 identical to sample 1 (cf. Fig. 1). One can see that, below the deep minima, there are maxima in the conductivity. This is evidence that the features appear in the density of electronic states;

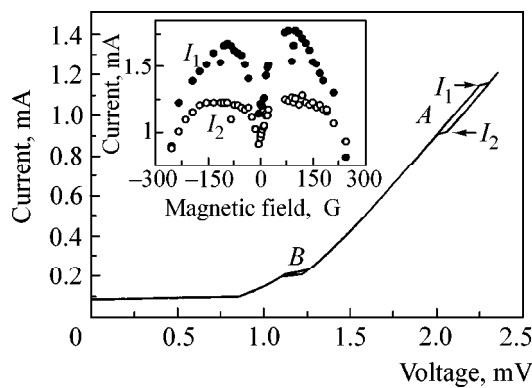---

[1] This article was submitted by the authors in English.
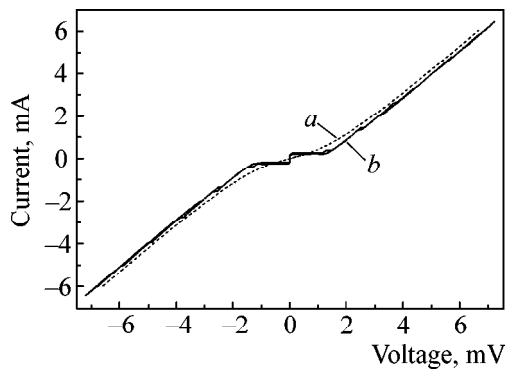
Fig. 1. Typical CVC of the Nb/Al–AlO$_x$–Al–AlO$_x$–Al–AlO$_x$–Al–AlO$_x$–Nb junction (sample 1) at *a*, $T = 4.2$ K and *b*, $T = 1.8$ K.

Fig. 2. First derivative $dI/dV(V)$ of the CVC measured for the 4-barrier junction (sample 2) at $T = 1.8$ K. The derivative was numerically calculated from the branch of the CVC recorded for increasing current.

Fig. 3. Initial part of the CVC of sample 2 at $T = 1.8$ K showing two features (*A* and *B*). Currents I_1 and I_2 denote the onset of the forward and backward voltage "jumps," respectively, for feature *A*. The inset shows the field dependence of currents I_1 and I_2 (solid and open circles, respectively).
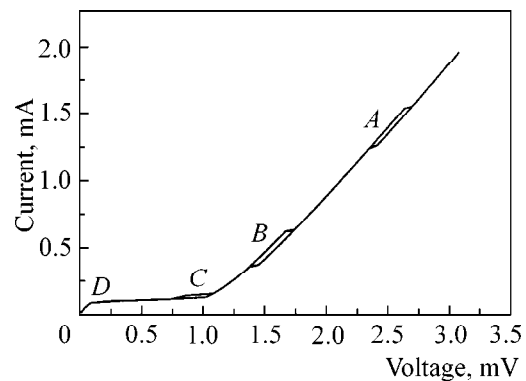
Fig. 4. Initial part of the CVC of sample 2 at $T = 1.8$ K in parallel applied magnetic field $H = 95$ G. Two additional features (*C* and *D*) are displayed (cf. Fig. 3).

i.e., some states are displaced from the minigaps to the maxima.

The new features are sensitive to a parallel applied magnetic field. They are significantly smeared at a field of $H \sim 300$ G. The voltage and the current at the positions of the voltage "jumps" also depend on the magnetic field. Figure 3 shows two of the features: *A* (at $V \approx 2$ mV) and *B* (at $V \approx 1.2$ mV) on an expanded scale for sample 2. Currents I_1 and I_2 denote the onset of the forward and backward voltage "jumps," respectively, associated with feature *A*. The inset in Fig. 3 shows field dependences of the currents I_1 and I_2, which have a minimum at H = 0 and resemble the field dependence of the height of the Fiske steps in ordinary SIS Josephson junctions [7]. This dependence is typical of the features under consideration. In fact, the magnetic field shifts the band structure along the *V* axis, so that, at some value of *H*, a new feature (*C*) appears at a low voltage $V \approx 1$ mV (see Fig. 4). Also, the resistive branch *D* near zero voltage is clearly seen. This resistive

branch is often masked by the Josephson current in the absence of an applied magnetic field (cf. Fig. 3).

Sensitivity to a weak magnetic field is strong evidence that the effect is related to the phase-coherent current. On first sight, it may be taken for the Tomash or Rowell–MacMillan effect [8–10]. However, these effects should be ruled out as possible explanations of the observed band structure due to the following major reasons: (i) We fabricated and measured many double-barrier SINIS devices with the same geometry of the S and N electrodes, but the effect was not present for such junctions. Therefore, it is apparently associated with the multiple-barrier structures. (ii) Both the Tomash and Rowell–McMillan effects produce oscillations of the junction conductance above the gap energy Δ_S of the S electrode and the conductance peaks due to bound states below that energy (the last statement is for the Rowell–McMillan effect only, because the Tomash oscillations are not present at the subgap energy). Unlike these effects, we observe a band structure that is a sequence of narrow conductivity hollows rather than peaks or nearly harmonic oscillations and has essen-

tially the same shape both below and above the Δ_S energy.

We suppose that the band structure is due to coherent transport between the external S electrodes through the ININI NI barrier and suggest the following interpretation of the new effect. It is known that a band structure may appear in the conductivity of systems involving a periodic potential [11]. In practical normal-metal–insulator multilayers, this structure, to our knowledge, has not been observed experimentally so far. Probably, this is due to the fact that it is difficult to fabricate homogeneous multilayers with very thin (a few atomic planes) films and perfect (on the atomic scale) interfaces to satisfy the interference conditions for the very short wavelength $\lambda_N \sim 1/p_F$ of the normal electrons (here, p_F is the Fermi momentum). In SINI…NIS structure with a not too low transparency of the insulating barriers, there is a finite probability of Andreev reflection at the SIN and NIS interfaces. For Andreev reflection, one may introduce a wavelength $\lambda_s \simeq 2\pi/q_s$ with $q_s = p_e - p_h \ll p_F$ (where p_e and p_h are the quasielectron and quasihole momenta, respectively) [2] The value of λ_s is of the order of the coherence length in the superconductor, ξ, and is much longer than the wavelength of normal electrons. Therefore, quasiparticle interference is possible in N films with a thickness of order ξ. This condition is satisfied in our experiments. For similar SINIS devices, we have observed coherent effects that may be associated with quasiparticle interference [3]. It is important (for the case described in [3] and the case considered here) that the tunnel barriers in the system are of "intermediate" strength, so that both Andreev and normal reflections take place. These two types of reflections give rise to constructive interference effects that may increase the conductivity of the devices at certain energies. However, even for a simple SINIS case, the electron spectrum of the system strongly depends on the particular setup and, in general, cannot be derived analytically. The situation is more complicated for a multiple INI..NI barrier. Numerical calculations for the ININI NI barrier were carried out recently by Shafranjuk [12]. It was found that the interference in this case may be destructive [12] and result in a band structure similar to that observed in our experiment. An optical analogue of this phenomenon may be found in stacks of alternating layers of semitransparent metal films and a dielectric material, where photonic band gaps were recently observed in transmittance [13].

REFERENCES

1. T. M. Klapwijk, Physica B (Amsterdam) **197**, 481 (1994).
2. I. P. Nevirkovets and S. E. Shafranjuk, Phys. Rev. B **59**, 1311 (1999).
3. I. P. Nevirkovets, J. B. Ketterson, and S. E. Shafranjuk, Physica B (Amsterdam) (in press).
4. G. Bastian, E. O. Göbel, A. B. Zorin, *et al.*, Phys. Rev. Lett. **81**, 1686 (1998).
5. O. Nesher and G. Koren, Phys. Rev. B **60**, 9287 (1999).
6. I. P. Nevirkovets, J. B. Ketterson, and S. Lomatch, Appl. Phys. Lett. **74**, 1624 (1999).
7. A. Barone and G. Paterno, *Physics and Applications of the Josephson Effect* (Wiley, New York, 1982).
8. W. J. Tomash, Phys. Rev. Lett. **15**, 672 (1965).
9. W. L. McMillan and P. W. Anderson, Phys. Rev. Lett. **16**, 85 (1966).
10. J. M. Rowell and W. L. McMillan, Phys. Rev. Lett. **16**, 453 (1966).
11. S. Flügge, *Practical Quantum Mechanics* (Springer-Verlag, Berlin, 1971).
12. S. E. Shafranjuk, Phys. Rev. B (in press).
13. M. Scalora, M. J. Bloemer, A. S. Pethel, *et al.*, J. Appl. Phys. **83**, 2377 (1998); M. J. Bloemer and M. Scalora, Appl. Phys. Lett. **72**, 1676 (1998).

================= **CONDENSED MATTER** =================

Phase Diagram and Skyrmion Energy
for Bilayer Heterostructures at Integer Filling Factors[1]

S. V. Iordanski and A. Kashuba

Landau Institute for Theoretical Physics, Russian Academy of Sciences, ul. Kosygina 2, Moscow, 117334 Russia
e-mail: iordansk@itp.ac.ru
Received March 30, 2000

The phase diagram of a bilayer heterostructure at integer filling factors was established using the hidden symmetry method. Three phases, namely, ferromagnetic, canted antiferromagnetic (CAP), and spin-singlet, were found. We confirm early results of Das Sarma *et al.* Each phase violates the $SU(4)$ hidden symmetry and is stabilized by anisotropy interactions. A charged excitation in the bilayer, i.e., a skyrmion, was found and its anisotropic energy gap was calculated. The gap has a prominent minimum in the CAP. © *2000 MAIK "Nauka/Interperiodica".*

PACS numbers: 75.70.Cn; 75.10.-b

Integer filling factors ν of the Landau level (LL) in heterostructure 2D electron gas (2DEG) are of special interest. Here, the ground state is nondegenerate and the Hartree–Fock approximation (HFA) can be applied with the accuracy limited only by a small ratio of the Coulomb interaction energy to the energy of cyclotron resonance. The ground state of a single layer at ν = 1 is a ferromagnet with the elementary excitations being spin excitons or spin waves. These are gapless [1] in the exchange approximation and do not interact with each other for vanishing momenta [2]. Both are consequences of exact symmetry under spin rotation. In [3], a special spin texture in a 2DEG ferromagnet, the skyrmion [4], was predicted as an elementary charged excitation. The energy of a neutral skyrmion–antiskyrmion pair is just a half of the spin exciton energy.

In a bilayer 2DEG, the HFA applies only in two cases. The first one corresponds to well-separated layers, which is a common setup in the experiment [5, 6]. Here, one starts from two single-layer ferromagnets and makes a perturbation expansion in powers of interlayer interactions [7]. The second one is the symmetric case, where the bilayer Hamiltonian is invariant under $SU(4)$ rotations in both layer and spin spaces. Here, all symmetry-breaking fields, like the Zeeman, must be negligible. The first attempt in this direction dealt with the case ν = 1 and spin-polarized electrons [8, 9]. Recent works [10, 11] that specialize to the bilayer case ν = 2 employ the HFA and predict three distinct phases: ferromagnetic, CAP, and a spin-singlet phase. Our approach is similar to that of [11], but we show explicitly that the HFA is exact in the $SU(4)$ symmetric bilayer. Anisotropy terms reduce the symmetry to $SU(2) \oplus SU(2)$ and lift the eigenstate degeneracy. But

there are no Fermi-liquid type renormalizations of the anisotropy Hamiltonian due to the symmetric Hamiltonian. We prove the stability of all phases with respect to long-range spatial perturbations. Our work was motivated by recent measurement of the diagonal conductivity activation energy in a bilayer [6], which we identify with the energy gap of a topological excitation, the skyrmion, in an $SU(4)$ Sigma model. The skyrmion's energy gap calculated in this letter has a profound minimum in the CAP, in line with the findings of [6].

The Hamiltonian of a 2DEG in a confining potential $V(\mathbf{\rho})$ and in an external magnetic field N has the form

$$H = \int \psi_\alpha^+(\mathbf{\rho})\left(\frac{1}{2m}[-i\mathbf{\nabla} + \mathbf{A}(\mathbf{\rho})]^2 + V(\mathbf{\rho})\right.$$

$$\left. - |g|\mu_B H \sigma_{\alpha\beta}^z \right)\psi_\beta(\mathbf{\rho})d^3\mathbf{\rho} \qquad (1)$$

$$+ \frac{1}{2}\iint \frac{e^2}{\kappa|\mathbf{\rho} - \mathbf{\rho}'|}\psi_\alpha^+(\mathbf{\rho})\psi_\beta^+(\mathbf{\rho}')\psi_\beta(\mathbf{\rho}')\psi_\alpha(\mathbf{\rho})d^3\mathbf{\rho}\, d^3\mathbf{\rho}',$$

where κ is the dielectric constant, α, β = ± are spin indices, and thereafter a sum over repeated indices is implied. We use the $\hbar = 1$, $e = c$, and $H = B = 1$ units and the distances are expressed in terms of the magnetic length $l_H = \sqrt{c\hbar/eH} = 1$. We split $\mathbf{\rho}$ into a coordinate ξ perpendicular to the layer and two in-plane coordinates $\mathbf{r} = (z, \bar{z})$ and assume the confining potential to be uniform over the plane $V(\mathbf{\rho}) = V(\xi)$, with the two wells being separated by a distance d. Two eigenfunctions, the lowest-energy symmetric and the lowest-energy antisymmetric, can be rotated into $\chi_{1,2}(\xi)$ eigenfunctions localized in one layer. We expand the electron operator in terms of these two eigenfunctions, $\psi_\alpha(\mathbf{\rho}) = \chi_\tau(\xi)\phi_p(\mathbf{r})c_{\alpha\tau p}$, where

---

[1] This article was submitted by the authors in English.

$c^+_{\alpha\tau p}$ and $c_{\alpha\tau p}$ are electron creation and annihilation operators and $\phi_p(z\bar{z})$ is the lowest LL wave function number p, the index $\tau = 1, 2$ being the layer index. We assume the case of a sufficiently strong magnetic field with the cyclotron energy $1/m$ dominating over the Coulomb, Zeeman, and the level splitting ($t = E_A - E_S$) energies.

The Coulomb interaction matrix can be projected onto $\chi_{1,2}(\xi)$:

$$
V^{\mu\nu}(\mathbf{r} - \mathbf{r}')
$$
$$
= \frac{e^2}{\kappa}\tau^\mu_{\tau_1\tau_4}\tau^\nu_{\tau_2\tau_3}\int\int\frac{\chi_{\tau_1}(\xi)\chi_{\tau_2}(\xi')\chi_{\tau_3}(\xi')\chi_{\tau_4}(\xi)}{\sqrt{(\xi - \xi')^2 + (\mathbf{r} - \mathbf{r}')^2}}d\xi d\xi' \quad (2)
$$

We use notations τ^0 for the unit matrix; τ^x, τ^y, and τ^z for the Pauli matrices in the layer space; and σ^x, σ^y, and σ^z for the Pauli matrices in the spin space. Coulomb energy (2) is invariant under transformations $\tau_1 \longleftrightarrow \tau_4$, $\tau_2 \longleftrightarrow \tau_3$, as well as $(\tau_1\tau_4) \longleftrightarrow (\tau_2\tau_3)$. Hence, $V^{\mu\nu}$ is a 3×3 symmetric matrix with indices μ, ν running over a set $(0, z, x)$. If there is a symmetry of the Coulomb interaction under an exchange of layers, $(\xi, \xi') \longleftrightarrow (-\xi, -\xi')$ and $1 \longleftrightarrow 2$, then it restricts further values of the interaction matrix: $V^{0z} = 0$ and $V^{zx} = 0$. We note also that $V^{0x} \sim t$, $V^{xx} \sim t^2$ and we neglect it thereafter, whereas $V^{zz} \sim d^2/|z|^3$ as $|z| \longrightarrow \infty$.

We split total Hamiltonian (1) into two parts. The first one is invariant under uniform rotations from the $SU(4)$ Lee group in the combined spin and layer space:

$$
H^{sym} = \frac{1}{2m}c^+_{\alpha\tau p}c_{\alpha\tau p}
$$
$$
+ \frac{1}{2}\int\frac{d^2\mathbf{q}}{(2\pi)^2}V^{00}(\mathbf{q})\exp\left(\frac{-\mathbf{q}^2}{4}\right)T^0(\mathbf{q})T^0(-\mathbf{q}), \quad (3)
$$

where (see, e.g., [9])

$$
T^\mu(\mathbf{q}) = \sum_p c^+_{\alpha\tau_1 p}\tau^\mu_{\tau_1\tau_2}c_{\alpha\tau_2 p - q_y}\exp\left\{-iq_x\left(p - \frac{q_y}{2}\right)\right\}. \quad (4)
$$

Its eigenlevels are hugely degenerate. Given any eigenstate $|\Psi\rangle_0$, a set of related eigenstates can be generated by applying rotations $|\Psi\rangle = U|\Psi\rangle_0$, where $U \in SU(4)$. For $\nu = 1, 2, 3$, we assume that the ground state is uniform over p orbitals:

$$
\Psi = \prod_{i=1}^{\nu}\prod_p c^+_{\alpha_i\tau_i p}|empty\rangle. \quad (5)
$$

Wave function (5) is an eigenfunction of H^{sym} (3). The second anisotropic part of Hamiltonian (1) is treated like a perturbation:

$$
H^{anis} = -c^+_{\alpha\tau_1 p}(t\tau^x_{\tau_1\tau_2} + \mu^z\tau^z_{\tau_1\tau_2})c_{\alpha\tau_2 p}
$$
$$
- |g|\mu_B H c^+_{\alpha\tau p}\sigma^z_{\alpha\beta}c_{\beta\tau p} \quad (6)
$$
$$
+ \frac{1}{2}\int\frac{d^2\mathbf{q}}{(2\pi)^2}V^{\mu\nu}(\mathbf{q})\exp\left(\frac{-\mathbf{q}^2}{4}\right)T^\mu(\mathbf{q})T^\nu(-\mathbf{q}).
$$

Here, t is the hopping constant. The electrostatic potential μ^z, which is the difference between chemical potentials in the two layers, breaks down the symmetry between the two wells of the $V(\xi)$ potential. We assume that the energy of a capacitor formed by the two layers is much lower than the characteristic Coulomb energy $e^2/\kappa l_H$. The Coulomb energy constants are

$$
E^{\mu\nu} = \int\frac{dz d\bar{z}}{2\pi l_H^2}V^{\mu\nu}(|z|)\exp\frac{-|z|^2}{2} \approx \int\frac{dz d\bar{z}}{2\pi}V^{\mu\nu}(|z|), \quad (7)
$$

where the last approximation holds for $(\mu\nu) \neq (00)$ in the limit $d \ll l_H$.

First, we specialize to the $SU(4)$-symmetric part of the bilayer 2DEG Hamiltonian (3). A weakly nonhomogeneous state is generated by a rotation matrix $c_{\alpha\tau} = U^{\alpha\beta}_{\tau\tau'}(t, \mathbf{r})c_{\beta\tau'}$, which adds a gauge matrix field $\Omega_\mu = -iU^+\partial_\mu U$ in the kinetic energy. An effective low-energy Goldstone action has an expansion in powers of Ω. We calculated this action following [12] step by step for $\nu = 1, 2, 3$ at once:

$$
H_G = \frac{E^1}{2}\int\frac{d^2\mathbf{r}}{2\pi}[\text{tr}((1 - N)\Omega_\mu N\Omega_\mu)
$$
$$
+ i\,\text{sgn}(B^z)\epsilon_{\mu\nu}\text{tr}(\Omega_\mu\Omega_\nu N)], \quad (8)
$$

where $E^1 = E^{00}/2$. The insertion matrices in Eq. (8) are nonnegative diagonal ones; and they represent the occupation number for the electron states

$$
N = \left(\begin{array}{c|c} 1 & 0 \\ \hline 0 & 0 \end{array}\right), \quad (9)
$$

where diagonal blocks are 1×1 and 3×3 in the case $\nu = 1, 3$ and 2×2 in the case $\nu = 2$. It can be proved that $H_G \geq 0$.

The matrices N and $1 - N$ are projector operators that allow only physical rotations in Hamiltonian (8) which do change the ground state. The vector field Ω_μ can be expanded in the basis of 15 generators of the $SU(4)$ Lee group. We subdivide them into two complementary sets: the first one includes generators that commute with N, constitute an algebra itself, and we called it a stabilizer subgroup S, whereas the remaining physical rotations constitute a coset $U(4)/U(\nu) \otimes U(4 - \nu)$ with dimension 8 in the case $\nu = 2$ and 6 in the case $\nu = 1, 3$.

Hamiltonian (8) is invariant under the time reversal symmetry, which can be chosen as a complex conjugate

operator $U \longrightarrow U^*$. It follows that $\Omega_\mu \longrightarrow -\Omega_\mu^T$. Thus, the time reversal changes the sign of the trace and the sign of the magnetic field B^z in the second term of Eq. (8).

The first term in H_G (8) is the gradient energy, whereas the second term is proportional to the topological index of a nonhomogeneous state:

$$\mathcal{Q} = \text{sgn}(B^z)\int \text{curl}\Omega^z \frac{d^2\mathbf{r}}{2\pi} = Z, \qquad (10)$$

where Z is the set of integer numbers. The case $\mathcal{Q} = \pm1$ corresponds to the simplest spin skyrmion in the first layer, being rotated by an $SU(4)$ matrix to become a general bilayer skyrmion. The energy constant in H_G (8) coincides identically with that of the one-layer case [12], which means that the bilayer skyrmion energy is the same as that found for a single layer.

We introduce a local bilayer order parameter $Q(\mathbf{r}) = U(\mathbf{r})NU^+(\mathbf{r})$, much like the magnetization in the theory of magnetism. Rotations from the denominator subgroup S leave Q intact. The total bilayer Hamiltonian in terms of this order parameter has the form

$$H_G = \frac{E_1}{4}\int \text{tr}(\nabla Q \nabla Q)\frac{d^2\mathbf{r}}{2\pi}$$
$$+ \text{sgn}(B^z)\frac{E_1}{2}\int \epsilon_{\mu\nu}\text{tr}(Q\partial_\mu Q\partial_\nu Q)\frac{d^2\mathbf{r}}{2\pi}. \qquad (11)$$

In this representation, the index selection rule (10) is a consequence of the homotopy group identity. Finally, we include the direct Coulomb energy of the charge inside a skyrmion core,

$$H_{ee} = \frac{1}{2}\iint d^2\mathbf{r} d^2\mathbf{r}' \frac{\text{curl}\Omega^z(\mathbf{r})}{2\pi}\frac{e^2}{|\mathbf{r}-\mathbf{r}'|}\frac{\text{curl}\Omega^z(\mathbf{r}')}{2\pi}. \quad (12)$$

We can recast the anisotropic part of the bilayer Hamiltonian (6) in terms of the order parameter matrix Q as well:

$$H^{anis}/\mathcal{N} = -(t + (\nu-1)E^{0x})\text{tr}(Q\tau^x)$$
$$- (\mu^z + (\nu-1)E^{0z})\text{tr}(Q\tau^z) - |g|\mu_B H\text{tr}(Q\sigma^z) \qquad (13)$$
$$+ \frac{1}{2}E^{zz}[\text{tr}(Q\tau^z)\text{tr}(Q\tau^z) - \text{tr}(Q\tau^z Q\tau^z)],$$

where $\mathcal{N}$ is the degree of degeneracy of the LL; τ^μ acts on the four-spinor as $\tau^\mu \otimes \sigma^0$. Eqs. (11)–(13) define the effective long-range Hamiltonian of a bilayer for integer ν.

The order parameter can be parametrized by six or eight angles in the case $\nu = 1, 3$ or $\nu = 2$. Actually, not all of these rotations correspond to a physically distinct eigenstate. The total bilayer energy is given by the real diagonal matrix elements. One generates all real eigenstates from a reference state by the rotations from the $SO(4)$ subgroup of the $SU(4)$ group. This group has six
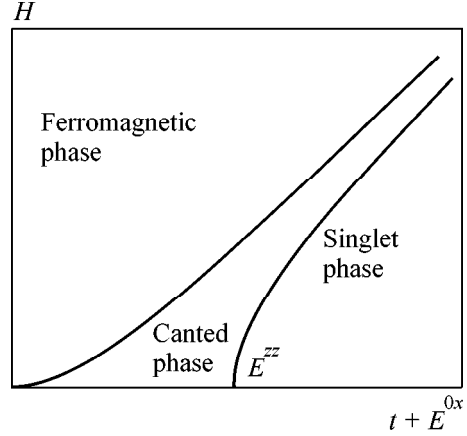

Fig. 1. Phase diagram in the $\nu = 2$ gate-symmetric case.

parameters, with two of them being from the stabilizer. Thus, only four global rotations change the total bilayer energy. We start with the case $\nu = 2$ and use a set of trial many-electron wave functions parametrized by the three angles of rotation relevant in our case, i.e., $\theta_\pm$ and ϑ:

$$\prod_p U(\vartheta, -\vartheta)R(\theta_+, \theta_-)c^+_{+1p}c^+_{-2p}|empty\rangle, \qquad (14)$$

where the $\pm$ spin components of the electron are first rotated by angles $\theta_\pm$ in the layer space and then the spins in the layer 1,2 are rotated by angles $\pm\vartheta$. Introducing $Q = URNR^+U^+$ into Eq. (13), we find

$$E^{anis}/\mathcal{N} = -E^{zz}\cos\theta_+\cos\theta_-$$
$$- (t + E^{0x})\cos\vartheta(\sin\theta_+ + \sin\theta_-)$$
$$- (\mu^z + E^{0z})(\cos\theta_+ - \cos\theta_-) \qquad (15)$$
$$- |g|\mu_B H\sin\vartheta(\cos\theta_+ + \cos\theta_-).$$

The minimum of this energy corresponds to three phases: a) ferromagnetic at $\vartheta = \pi/2$, $\theta_+ = \theta_- = 0$; b) spin singlet at $\vartheta = 0$, $\theta_+ = \pi - \theta_- = \theta$; and c) CAP otherwise, as is shown in Fig. 1. A line of continuous phase transitions between the ferromagnetic phase and CAP is given by

$$[(E^{zz} + |g|\mu_B H)^2 - (\mu^z + E^{0z})^2]|g|\mu_B H$$
$$= (t + E^{0x})^2(E^{zz} + |g|\mu_B H). \qquad (16)$$

In the spin-singlet phase, the mixing phase θ is determined by the equation

$$(E^{zz}\sin\theta + t + E^{0x})\cos\theta = (\mu^z + E^{0z})\sin\theta. \qquad (17)$$

A line of continuous phase transition between the spin-singlet phase and CAP is given parametrically by the
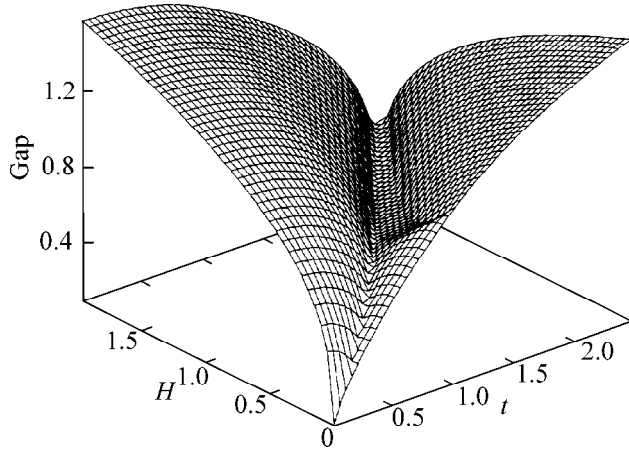
Fig. 2. Total anisotropic anti skyrmion gap energy in the $\nu = 2$ gate-symmetric case.

equation

$$((t + E^{0x})\sin\theta - E^{zz} + (\mu^z + E^{0z})\cos\theta)(t + E^{0x}) = (|g|\mu_B H)^2 \sin\theta, \quad (18)$$

with θ being determined from Eq. (17). In the case $\nu = 1, 3$, there is only one phase which is ferromagnetic in both spin and layer spaces.

Next, we find the skyrmion energy. The skyrmion's order parameter is given by the Belavin–Polyakov (BP) solution for $|\mathcal{Q}| = 1$ [4]

$$Q_{BP}(z\bar{z}) = \frac{R^2}{R^2 + |z|^2}\left(\frac{|z|^2}{\bar{z}R}\bigg|\frac{zR}{R^2}\right), \quad (19)$$

with only a single free parameter, the radius of the skyrmion core R. We omit the unessential rotation angle between spin and orbital frames, arbitrary in the absence of spin–orbit interaction. This Q has to be rotated by a homogeneous matrix RU (see above) in order to minimize the anisotropy energy away from the core. In addition, we allow all homogeneous rotations W from the stabilizer S that transform the BP skyrmion solution (19): $Q(\mathbf{r}) = RUWQ_{BP}(z\bar{z})W^+U^+R^+$.

We retain only logarithmically divergent spatial integrals and numerically calculate the minimum of the skyrmion anisotropy energy over the seven free parameters of matrix W, $\mathcal{E}_{min}^{skyr}$. Then, we add the direct Coulomb energy (12) and minimize the total skyrmion

energy with respect to R:

$$\Delta = \frac{\mathcal{Q} + |\mathcal{Q}|}{2}E_1$$

$$+ 3\left(\mathcal{E}_{min}^{skyr}\left(\frac{3\pi^2 e^2}{128\kappa l_H}\right)^2 \log\frac{e^2}{\kappa l_H \mathcal{E}_{min}^{skyr}}\right)^{1/3}. \quad (20)$$

In the case of an antiskyrmion $\mathcal{Q} = -|\mathcal{Q}|$, the gap consists only of a relatively small anisotropic energy. The total anisotropic skyrmion gap is shown in Fig. 2 for the gate-symmetric case $\mu^z + E^{0z} = 0$. Note that the two cusplike lines coincide with the two phase-transition lines in Fig. 1. A skyrmion in the ferromagnetic phase is a spin skyrmion, with spin rotations being localized in one layer, whereas a skyrmion in the spin-singlet phase is a layer skyrmion, with the electron density being rotated into the other layer.

In the case $\nu = 1, 3$, we find the minimum of skyrmion's energy to be

$$\Delta = \frac{\mathcal{Q} + |\mathcal{Q}|}{2}E_1 + \min(2\sqrt{t^2 + \mu_z^2}, 2|g|\mu_B H). \quad (21)$$

REFERENCES

1. Yu. A. Bychkov, S. V. Iordanski, and G. M. Eliashberg, Pis'ma Zh. Éksp. Teor. Fiz. **33**, 152 (1981) [JETP Lett. **33**, 143 (1981)].
2. I. V. Lerner and Yu. E. Lozovik, Pis'ma Zh. Éksp. Teor. Fiz. **82**, 1188 (1982) [Sov. Phys. JETP **55**, 691 (1982)].
3. S. Sondhi, A. Kahlrede, S. Kivelson, and E. Rezai, Phys. Rev. B **47**, 16419 (1993).
4. A. A. Belavin and A. M. Polyakov, Pis'ma Zh. Éksp. Teor. Fiz. **22**, 245 (1975) [JETP Lett. **22**, 114 (1975)].
5. V. Pellegrini *et al.*, Phys. Rev. Lett. **78**, 310 (1997).
6. V. S. Khrapai *et al.*, Phys. Rev. Lett. **84**, 725 (2000).
7. S. Das Sarma, S. Sachdev, and L. Zheng, Phys. Rev. Lett. **79**, 917 (1997).
8. M. Rasolt, B. Halperin, and D. Vanderbilt, Phys. Rev. Lett. **57**, 126 (1986).
9. Yu. A. Bychkov and S. V. Iordanski, Fiz. Tverd. Tela (Leningrad) **29**, 2442 (1987) [Sov. Phys. Solid State **29**, 1405 (1987)].
10. L. Zheng *et al.*, Phys. Rev. Lett. **78**, 2453 (1997); S. Das Sarma *et al.*, Phys. Rev. B **58**, 4672 (1998); E. Demler and S. Das Sarma, Phys. Rev. Lett. **82**, 3895 (1999).
11. A. H. MacDonald, R. Rajaraman, and T. Jungwirth, Phys. Rev. B **60**, 8817 (1999).
12. S. V. Iordanski, S. G. Plyasunov, and V. I. Falko, Zh. Éksp. Teor. Fiz. **115**, 716 (1999) [JETP **88**, 392 (1999)].

Information for Authors

PACS numbers: 01.30.-y

The journal *Pis'ma Zh. Éksp. Teor. Fiz.* (and its English edition *JETP Letters*) publishes short papers that need to be urgently published and are of broad physical interest. These papers should report first observations of new physical phenomena or new fundamental theoretical results.

This journal accepts and publishes manuscripts submitted in Russian or English. All manuscripts submitted in English are put to a linguistic test. If the English text appears unreadable, the Editorial Board may request that the authors submit the Russian variant of the manuscript for publication.

All articles in *JETP Letters* are published in English. The translation of manuscripts submitted in Russian, as well as the editing of manuscripts submitted in English, is performed by the International Academic Publishing Company (IAPC) "Nauka/Interperiodica."

The total length of any paper should not exceed six journal pages in the Russian edition. This length approximately corresponds to 20 KB in *LATeX* format, including 1 KB for each figure. You can estimate the manuscript length more accurately by preparing it according to an example that is available on the Web server for the journal (http://kapitza.ras.ru/journals/jetpl) by using the style file (jetpl.sty) available on the same server.

Manuscripts may be submitted to the Editorial Board in the following ways:

(1) Conventional mail to the following address: *Pis'ma Zh. Éksp. Teor. Fiz.*, ul. Kosygina 2, Moscow, 117334 Russia. The manuscript should be submitted in duplicate with figures on separate sheets (for half-tone figures, one additional copy should be submitted). Please append the e-mail and postal addresses (including the postal code), the office and home phone numbers, and the complete name and patronymic of the author to whom correspondence should be addressed. The authors of English manuscripts should also submit a floppy disk containing the text in the *LATeX* format.

(2) Electronic mail to the e-mail address letters@kapitza.ras.ru. In this case, each figure should be submitted in the form of an individual file in PostScript (*.ps), EncapsulatedPostScript (*.eps), or PaintBrush (*.pcx) formats.

Acceptance or rejection of a paper for publication is decided by the Editorial Board with a proposal from the Editorial Board member specialized in the appropriate section. A manuscript can be rejected if it is not topical enough, does not provide considerable development as compared to other publications in this field, considers a too specific subject, etc. As a rule, the referee reports on rejected papers are not sent. The authors may resubmit a rejected manuscript, appending it with an explanatory letter. In this case, the manuscript will be put under additional review.

The Editorial Board sends (or hand delivers if the authors live in Moscow) five reprints of the papers published in the Russian edition. The English version is sent to the authors in electronic mode by IAPC "Nauka/Interperiodica."

MANUSCRIPT PREPARATION

The first page of a manuscript should have the following form:

THE TITLE

Initials and Surnames of the Authors

Institutions where the authors work, including city and postal code (the e-mail address of one of the authors is desirable)

Text of the Abstract

PACS: … (Physics and Astronomy Classification Scheme, see Pis'ma Zh. Éksp. Teor. Fiz. **58** (7 and 9), (1993) [JETP Lett. **58** (7 and 9), (1993)]).

Then, after one empty line, the main text follows.

Because abstracts may now be distributed separately from the papers (data bases, online systems, etc.), the abstract text should be self-contained with no references or abbreviations but with understandable notation.

Abbreviations must be given in capital letters with no points and should be explained as they are first introduced. Footnotes in the main text must be numbered consecutively in the order of their appearance.

Cited references must be given in a general list at the end of a manuscript and should be numbered with an ordinal number (e.g., [1]) consecutively as they are mentioned in the main text. The reference to a journal article should cite the following: the initials and surnames of the authors, journal name, volume number (in boldface type), the first page of the paper, and year enclosed in parentheses. If an article is written by more than four authors, indicate only the first three, e.g.,

1. A. B. Ivanov, V. G. Petrov, I. M. Sergeev, *et al.*, Zh. Éksp. Teor. Fiz. **98**, 290 (1990) [JETP **71**, 161 (1990)].

References to books must cite the following: the initials and surnames of the authors, the complete book title, and year and place of publication (in the case of translated books, give the information for the original in parentheses).

Use decimal points instead of commas. Three-vectors and dyadics with no arrow above them must be underlined with blue pencil.

We recommend that authors preparing figures electronically adhere to the following rules: prepare figures in the frame; direct dashes on the axes inside the figure; when possible, use Arial font; use numerals (including those on the axes in an insert) and lower case letters with a height of 3–4% of the maximum figure size (height or width) of the figures; put measurement units on the axes in parentheses.

Examples of the preparation of manuscript and figures, as well as a style file, are available on our Web server (http://kapitza.ras.ru/journals/jetpl).

The English variant proof is sent (via e-mail) to the author for agreement for a span of five days. If the author does not agree with the terminology used or decides that the translation of some sentences distorts their semantic meaning, he submits his proposals for changes. The author should not intrude into the linguistic aspect of the translation. The absence of an answer from the author in above-indicated time is considered as the author's agreement with the text. If the author has no criticisms, he should inform the publisher about his agreement.

Translated by R. Tyapaev